

Dear Referees,

First of all, I'd like to thank you for your time and providing helpful comments that have improved the quality of this manuscript. In the following, I am responding point-by-point to each of your remarks in green letters. The corresponding changes were included with mark-ups in the final version of the manuscript (see below).

On behalf of the authors,

best regards,

Jörg Alber

### **Point-by-point reply to Referee #1 (RC1, Galih Bangga)**

Received: 10<sup>th</sup> of August 2020

Dear Authors,

The investigated studies are of interest for wind turbine community and have been conducted thoroughly. After evaluating your paper and previous remarks from the reviewers, I agree with most of your answers but further detail shall be given concerning the angle of attack. Below please find some minor critics that I wish to be considered before the paper can be published:

1. If I follow your paper correctly and by reading your answers to one of the reviewers (including the paper from Annette), the angle of attack was obtained in the measurement by assuming 2D flow. This was done by comparing the rotating rotor with a 2D polar data. This relatively simple approach should work well if no flow separation or unsteady effect presents. However, as you introduce the Gurney flaps, there will be little unsteadiness occurring near the trailing edge of the blade. How did you take this into account?

In this paper, no 2D airfoil assumptions or simulations have been used for any of the AoA calculations. The AoA is obtained experimentally by means of the axial and tangential wake velocities (Sect. 3.1). The only 2D flow assumptions were used to estimate the boundary layer thickness in order to determine the height of both the ZZ-tape and the GFs (with XFOIL).

Previously, Annette Klein et. al. published experiments on the BeRT using a 3-hole probe set-up (p.446) in the mid-span region ( $r=0.65R$ ). For that, 2D polar data ( $cl$ ) was used in order to calculate the AoA. These previous investigations are used as a reference to the tests that are published in this new paper.

Considering the question at the end: there are numerous publications showing that Gurney Flaps (GFs) lead to increased unsteadiness near the trailing edge. This is the main reason for drag increase. However, the more the GF is submerged "deep enough" into the boundary layer (i.e. the smaller it is), the less pronounced is the unsteadiness that appears (see Fig. 2). Regarding the unsteadiness caused by the GF configurations that were tested in this campaign, the 3D Ultrasonic measurements in the wake do not reveal increased turbulence levels, see Fig. 7 (b).

2. The source of the 2D polar data for the AoA calculation is also unclear. Was the Gurney flap also included here?

No 2D polar data has been used for the calculations of the presented results. The only (external) 2D lift polars are presented as a reference to our results, see Fig. 12.

3. Furthermore, the analysis was done mostly at 0.45R, and you claimed that the AoA evaluation has been confirmed with FLOWer calculations in the other paper. Despite that, the comparison done in Annette's

paper was at the spanwise positions no less than  $0.65R$ . How did you ensure the 2D assumption will be correct especially for the lower TSR case? I do agree that lift will not be affected significantly for little inaccuracy in AoA calculation in the mid-span region, however drag will still be influenced as I have seen for example on the AVATAR rotor (see Fig. 7 page 13 <https://aip.scitation.org/doi/pdf/10.1063/1.4978681>).

The blade positions with respect to the measurement methods were clarified in the revised version of the manuscript, see the new Table 3.

The assumption of constant AoA throughout the mid-span region ( $0.45R < r < 0.65R$ ) is explained in more depth (see new Table 4)

However, it is not possible to measure the total drag coefficients ( $c_d$ ) of any blade-element of the BeRT, see following comment no. 4 and 5.

4. It is interesting to note that you state the drag penalty is still at reasonable value (line 115) but this has never been proven in the paper.

This statement is a generally accepted design-consideration by numerous airfoil experiments and/or CFD simulations: the airfoil drag,  $c_d$ , increases in relation to the GF height. Vice versa, the more the GF is submerged by the BL layer, the smaller the drag-increase becomes (see Sect. 1).

This statement was clarified in the new version of the manuscript. In addition, the experimental results of the pressure drag were included, see following comment 5.

5. Lastly, I would recommend to add a plot showing the lift over drag to really assess the performance of the rotor. The drag might be estimated by the pressure integration, although friction drag is also important for small AoAs.

The tangential force coefficient,  $c_t$ , can be transformed into the pressure-drag component,  $c_{d,p}$ , which does not include the skin-friction drag component (see Sect. 2.3.2). Hence, presenting only the values for pressure-drag is, by default, incomplete information.

As suggested, the plots of the pressure drag ( $c_l$  over  $c_{d,p}$ ) plus explanations were included as an indicator for the drag performance of the blade element, with and without the use of GFs, see Sect. 3.2.

Small typos

Line 275 i.e.  $0.65R < r < 0.45R$  --> should be other way around.

Done.

Line 13 Reynold --> Reynolds. It is a person name and please check for some others....

Done.

God luck!

Thank you!

Kind regards,  
Galih Bangga

## Point-by-point reply to Anonymous Referee #2 (RC2)

Received 10<sup>th</sup> of August 2020

The manuscript presents an experimental study on a 3 m diameter horizontal wind turbine rotor. The focus was on the effects of Gurney flaps on the aerodynamic performance of the blade. Two Gurney flaps heights were tested on a clean blade and with turbulator tape.

Experiments studies are always welcome, whether for the knowledge provided and/or for data generated that can be used to validate numerical models.

Only few attempts to physically comment the experimental observations reported. This should be improved in the revised version of the manuscript.

My comments and suggestions are presented as follows:

1. A linguistic revision of the manuscript is recommended.

Done.

2. The introduction needs to be improved to show the relevance of the presented experiment. Can author briefly mention what are the wide knowledge gaps and what portion of that current study is trying to fill. List point-by-point objectives and map the achievements of objectives in conclusion.

The objectives and the relevance of the study were specified in both introduction and conclusions.

3. Line 38: add (c) after chord-length.

Done.

4. Line 48: correct the range ( $1.3 \%c < GF < 3.5 \%c$ ).

Done.

5. Line 87: the authors stated a blockage ratio of approximately 40 %. Could authors elaborate on this (how did they evaluate this value; what impact will have this blockage on the results...)

The definition of the blockage ratio was specified. Otherwise a reference to Sect. 3.1 (results) was included, where the effects of blockage are discussed in more depth.

(In general, the most tangible effect of the wind tunnel blockage is the fact that the axial wake velocity is much higher than expected. As a direct consequence, the AoA are elevated, too.)

6. Line 109: mention that XFOIL is a program.

Done.

7. Section 2.2.1-2.2.2: To adjust the dimensions of the ZZ tape and the GF, the authors used XFOIL to evaluate the BL thickness. XFOIL is a 2D airfoil calculator, could authors explain how can exploit this result to a blade flow which is 3D?

The sections were rewritten clarifying that the flow is attached (pre-stall) and thus assumed 2D in order to estimate the BL-thickness by means of the XFOIL code.

8. Please rearrange Table 1 for clarity. Tripped case is missed. Measurement method part could be arranged in another table.

The tables were split up and rearranged for more clarity, as suggested: see new Table 1, 2 and 3.

9. Lines 138-139: the authors stated that their findings are relevant beyond the Re-numbers of the BeRT blades, as long as the GF/BL ratio is kept constant. Are you suggesting that 2 flows with different Re numbers are comparable? Please explain more about this statement and define the ratio (GF/BL) in the text.

This statement was shifted to Sect. 2.2.2 (dimensioning of GF-height), where it fits better than in combination with the test matrix. The design concept of the GF/BL-ratio was explained in depth and with more clarity.

10. Line 217: RMBs#RBM

Done.

11. Curves in graphs with 2 vertical axes must be correctly identified. For example, in figure 7a, indicate which curves correspond to axial and tangential velocities.

Done.

12. Line 245: free flow conditions may be confusing (flow without turbine or without wind tunnel walls).

Done.

13. Lines 245-253: The authors showed that the axial wake velocity is more sensitive to the wind tunnel blockage than the tangential velocity, could you please explain this phenomenon?

The tangential velocity-component depends primarily on the rotational speed of the blade. Hence, it is less affected by the rapid axial velocity component. This observation was commented on in more depth.

14. Line 276: Define  $\Delta\alpha_{GF}$

Done.

15. Line 277: Please what do you mean by "to a more favourable level in terms of the BeRT rotor"? I think it is better to reformulate lines 277-278.

The statement was reformulated in order to make this point clearer.

(The reason why the BeRT performance is improved by the GFs is because it is running sub-optimally due to the wind tunnel blockage effects and/or ZZ tape. Otherwise, if BeRT ran at its optimum, the impact of GFs would probably have an adverse effect on the performance)

16. Is there a reason to evaluate the angle of attack at  $r=0.56R$  and the pressure coefficient which depends on this angle at a different radial position ( $r=0.45R$ )?

The (practical) reason is that the AoA were evaluated by different experiments at different span-wise positions along the mid-span area:

- 0.45R -> pressure tabs (reference to Soto-Valle et al.)
- 0.56R -> Ultrasonic Anemometer
- 0.65R -> 3-hole probes (reference to Klein, et. al).

The new table 4 summarizes the different research efforts with more clarity.

Based on the mentioned results, the AoA are assumed constant in the mid-span area for  $0.65R < r < 0.45$  (due to the built-in twist angles of the blades). This assumption was explained in a clearer way in the new version of the manuscript.

17. Line 285: Define  $\Delta C_p$ .

Done.

18. Lines 285-290: Description of Figure 10 needs to be rewritten more clearly to show the effect of GF on the pressure coefficient.

Done. The paragraph in question was re-written.

19. Line 312: change  $\Delta c_l$  to  $c_l$ .

Actually, the purpose of Fig. 12 is the comparison between both  $c_l$  and  $\Delta c_l$ , i.e. the  $c_l$  of the baseline and the shift of  $\Delta c_l$  when implementing a GF. The statement was rephrased for clarification.

20. Regarding the conclusion, please see comment #2.

The conclusions were re-written in accordance with the suggested changes from comment #2.

# Aerodynamic Effects of Gurney Flaps on the Rotor Blades of a Research Wind Turbine

Jörg Alber<sup>1</sup>, Rodrigo Soto-Valle<sup>1</sup>, Marinos Manolesos<sup>2</sup>, Sirko Bartholomay<sup>1</sup>, Christian Navid Nayeri<sup>1</sup>,  
Marvin Schönlau<sup>1</sup>, Christian Menzel<sup>1</sup>, Christian Oliver Paschereit<sup>1</sup>, Joachim Twele<sup>3</sup>, Jens Fortmann<sup>3</sup>

<sup>1</sup> Technische Universität Berlin, Hermann-Föttinger Institut, Müller-Breslau-Str. 8, 10623 Berlin, Germany

<sup>2</sup> College of Engineering, Swansea University, Bay Campus, Fabian Way, Swansea, SA1 8EN, United Kingdom

<sup>3</sup> Hochschule für Technik und Wirtschaft Berlin, Wilhelminenhofstraße 75A, 12459 Berlin, Germany

Correspondence to: Jörg Alber (joerg.alber@htw-berlin.de)

## Abstract.

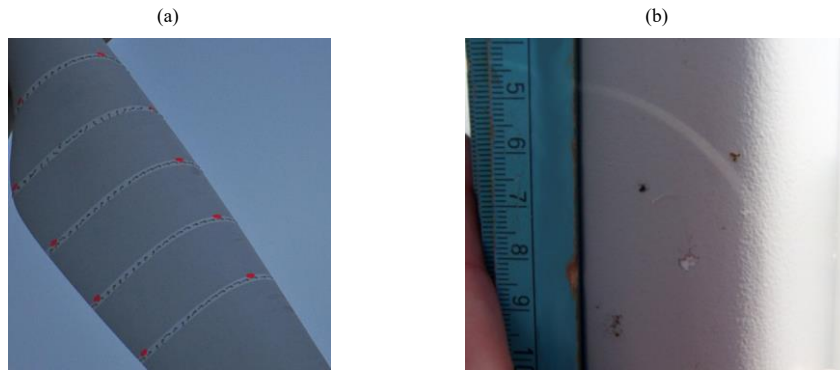
10 This paper investigates the aerodynamic impact of Gurney flaps on a research wind turbine of the Hermann-Föttinger Institute  
at the Technische Universität Berlin. The rotor radius is 1.5 meters and the blade configurations consist of the clean and the  
tripped baseline cases emulating the effects of forced leading edge transition. The wind tunnel experiments include three  
operation points based on tip speed ratios of 3.0, 4.3 and 5.6, reaching Reynolds numbers of approximately  $2.5 \cdot 10^5$ . The  
15 measurements are taken by means of three different methods; Ultrasonic Anemometry in the wake, surface pressure taps in  
the mid-span blade region and strain gauges at the blade root. The retrofit applications consist of two Gurney flap heights of  
0.5 % and 1.0 % in relation to the chord length, which are implemented perpendicular to the pressure side at the trailing edge.  
As a result, the Gurney flap configurations lead to performance improvements in terms of the axial wake velocities, the angles-  
of-attack and the lift coefficients. The enhancement of the root bending moments imply an increase of both the rotor torque  
and the thrust. Furthermore, the aerodynamic impact appears to be more pronounced in the tripped case compared to the clean  
20 case. Gurney flaps are considered a passive flow-control device worth investigating for the use on horizontal axis wind  
turbines.

## 1 Introduction

The energy yield of modern Horizontal Axis Wind Turbines (HAWTs) is supposed to be optimal while keeping the  
maintenance costs as low as possible over a lifetime of around 20 years. However, the performance of rotor blades faces serious  
25 challenges, two of which are early separation and roughness effects. Early separation is a problem especially in the inner blade  
region towards the root where the Angles-of-attack (AoA) are elevated due to structural constraints, such as limited chord-  
length and twist-angles, see Figure 1 (a). Over time, the resulting dynamic loads contribute to the material fatigue of the blade  
(Mueller-Vahl et al., 2012). For this reason, Passive Flow Control (PFC) devices, such as Vortex Generators (VGs), are  
implemented in the inner blade region of different-size HAWTs aiming at stall delay (Pechlivanoglou et al., 2013). At the

Kommentiert [D1]: RCI: typo

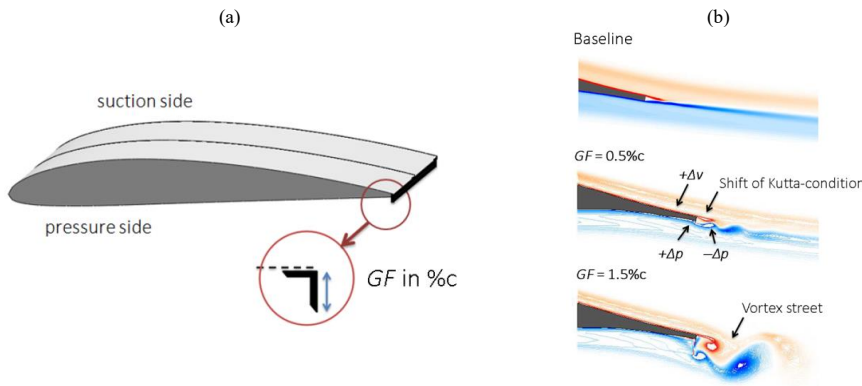
30 same time, the longstanding surface erosion causes roughness effects, especially close to the Leading Edge (LE), see Figure 1 (b). LE roughness is relevant throughout the entire blade span and especially in the outer region towards the blade tip. Apart from the broad range of weather conditions, surface roughening is aggravated by rain, insects as well as sand or salt particles. Consequently, the energy yield of HAWTs is often found lower than predicted or regressing over time (Wilcox et al., 2017).



35 **Figure 1.** Rotor blades of utility scale wind turbines. (a) Flow indicators to detect early separation in the inner blade region, reproduced from Pechlivanoglou et al. (2013). (b) Leading edge roughness, reproduced from Pechlivanoglou et al. (2010).

This paper investigates the retrofit application of Gurney Flaps (GFs) in order to improve the aerodynamic performance of rotor blades. This PFC device consists of a wedge- or right-angle profile that is attached perpendicular to the pressure side at the Trailing Edge (TE). The GF-height,  $GF$ , in relation to the chord-length,  $c$ , is the main design parameter, illustrated in [Figure 2](#) (a). It is usually in the range of  $0.5\%c < GF < 2.0\%c$  without taking the TE thickness into account.

**Kommentiert [D2]:** RC2, #3: add c  
**Formatiert:** Schriftart: Kursiv



40 **Figure 2.** (a) Position of the Gurney flap at the trailing edge of a Clark-Y airfoil section. (b) CFD simulation of the HQ17 airfoil at  $Re = 1.0 \cdot 10^6$ , reproduced and modified from Schatz et al. (2004).

The research on TE flaps of airplane wings dates back to the early 20<sup>th</sup> century (Gruschwitz and Schrenk, 1933). The GF itself is named after the racecar driver Dan Gurney who discovered the significant gain in downforce when applying the device on the rear spoilers. Following from that, GFs have been implemented on high-lift dependent transport airliners (Bechert et al., 2000) and helicopter stabilizers (Houghton et al., 2013). More recently, Vestas® has started offering GFs in combination with VGs as so-called aerodynamic upgrades of HAWTs, predicting annual yield improvements of up to 2.0% (Vestas, 2020). The design of the DTU 10 MW Reference Wind Turbine includes smooth wedge-shaped GFs in the first half of the blade length,  $0.05R < r < 0.4R$ , using GF-heights in the range of  $3.5\% < GF < 1.3\%$  ~~1.3% < GF < 3.5%~~ (Bak et al., 2013).

Kommentiert [D3]: RC2, # 4: correct expression

Figure 2 (b) illustrates the changes in the flow field of the laminar airfoil HQ17 when implementing different GF-heights, as reported by Liebeck (1978) by means of the Newman airfoil. Key to the aerodynamic understanding is the development of one vortex upstream and two counter-rotating vortices downstream of the GF, as such entailing a low-pressure region in the TE wake. As a result, the downwash angle of the flow becomes steeper, the requirements for pressure recovery on the suction side milder, the local boundary layer thinner and the suction peak higher. Additionally, the flow on the pressure side decelerates leading to a positive pressure built-up in the TE region. The resulting shift of the Kutta-condition leads to increased circulation and thus to elevated lift forces, which is the main Gurney flap characteristic. At the same time, the low-pressure region aft the TE induces additional drag, especially if vortex shedding is initiated in the form of a Kármán vortex street. Hence, the lift increase is accompanied by a certain drag penalty that affects the Lift-to-Drag (L/D) ratio accordingly.

~~That~~ This is why various experimental and numerical research projects aim at limiting the adverse drag increase while maintaining the beneficial lift enhancement of GFs. Giguère et al. (1995) and Kentfield (1996) conclude that the GF-height is supposed to be submerged into the local Boundary Layer (BL) in order to keep the drag on an acceptable level. Bechert et al. (2000) demonstrate that additional holes, slits and especially the pattern of dragonfly wings lead to reduced drag on the HQ17 airfoil ( $\eta_{max} = 15.2\%$ , at  $Re = 1.0 \cdot 10^6$ ). In addition, promising results are presented for very small GF-heights in the range of  $0.2\% < GF < 0.5\%$ , i.e. substantially smaller than the BL thickness at the TE. Following from that, CFD-based wake simulations of Schatz et al. (2004) reveal that the amount of induced drag depends on the GF-height, in fact, in a disproportionate manner, as illustrated in Figure 2 (b); ~~As such,~~ for  $GF = 1.5\%$  a vortex street is triggered, while for  $GF = 0.5\%$  the wake is shed in a relatively smooth way. In a similar manner, Alber et al. (2017) suggest the use of very small GF-heights of approximately half the local BL thickness in order to maintain, or even improve, the airfoil L/D-ratio of different DU and NACA airfoils.

Formatiert: Schriftart: Kursiv

Formatiert: Schriftart: Kursiv, Tiefgestellt

The aforementioned design principles,  $GF < \delta$ , are applied on the rotor blades of the Berlin Research Turbine (BeRT) research turbine using GF-heights of 0.5% and 1.0%. In addition, forced LE transition is triggered in order to emulate the effects of leading edge roughness.



roughness effects. Subsequently, the aerodynamic impact of retrofit GFs is investigated based by means of on the following experiments measurement methods:

- 3D Ultrasonic Anemometry in the turbine wake to determine the local AoA.
- Chord-wise P pressure taps in the mid-span blade region to determine calculate the local pressure distribution and the lift performance.
- Strain gauges at the blade root to determine measure the flapwise and the edgewise root bending moments.

In summary, the objective of the experiments is to assess the suitability of retrofit GFs in order to alleviate the following adverse effects:

- Early separation due to the high AoA regime, relevant in the inner blade region, see Figure 1 (a).
- Decreasing lift forces due to leading edge erosion, relevant in the outer blade region, see Figure 1 (b).

In the remaining of this paper, the experimental set-up is described in detail, followed by the presentation and the discussion of the results. The main conclusions are summarized in the final section of this report.

## 2 Experimental set-up

### 2.1 Berlin Research Turbine

The Berlin Research Turbine (BeRT) is a test bench of the closed-loop wind tunnel of the Hermann-Föttinger Institut at the Technische Universität Berlin. It is a unique wind turbine demonstrator to explore specific fluid-dynamic phenomena based on a fully equipped rotating system, as detailed by (Vey et al., (2015).

(a)

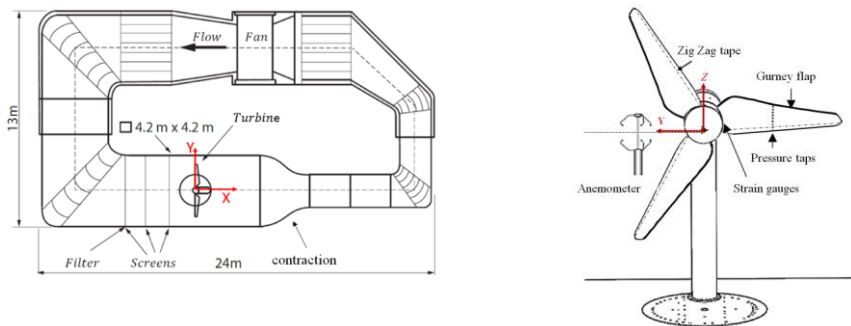
(b)

Formatiert: Listenabsatz, Abstand Nach: 0 Pt., Aufgezählt + Ebene: 1 + Ausgerichtet an: 0.63 cm + Einzug bei: 1.27 cm

Formatiert: Abstand Nach: 0 Pt.

Formatiert: Listenabsatz, Aufgezählt + Ebene: 1 + Ausgerichtet an: 0.72 cm + Einzug bei: 1.36 cm

Kommentiert [D4]: RC2, #2 and #20: specify objectives and relevance of experiments in both introduction and conclusions



95 **Figure 3.** (a) Closed-loop wind tunnel in top-view. (b) BeRT set-up in front-view looking downstream.

100 **Figure 3** (a) depicts the wind tunnel facility consisting of the high speed ( $(2.0 \times 1.4) \text{ m}^2$ ) and the low speed ( $(4.2 \times 4.2) \text{ m}^2$ ) test section. The BeRT is situated in the low speed test section downstream of the flow-conditioning screens and upstream of the wind tunnel contraction. The maximum inflow velocity is  $10 \text{ ms}^{-1}$ . The third screen upstream the rotor plane is equipped with an additional turbulence filter mat (Vildedon P15/150s) in order to reduce the turbulence intensity to  $1.0\% < Ti < 1.5\%$ , previously as reported by Bartholomay et al. (2017). **Figure 3** (b) displays the BeRT set-up and the measurement methods applied. The rotor radius is  $R = 1.5 \text{ m}$  producing a relatively large blockage ratio of approximately 40% in relation to the test section area. The blockage effects on both the flow and the rotor performance are discussed in Sect. 3.1. Relative distances are expressed in relation to the rotor radius,  $R$ , and the zero position at the center of the rotor plane at  $X = Y = Z = 0$ . The blades consist of the low Reynolds-profile, Clark-Y, with a maximum thickness of  $th_{max} = 11.9\%c$  and a modified TE thickness of  $0.75\%c$ . The blade geometry is optimized aerodynamically including a linear decrease of both the chord-lengths and the twist-angles from root to tip alongside most of the blade span. The root section is contiguous to the round rotor hub and the tip section is pointy, see **Figure 4**. The tip speed ratio at rated conditions is  $TSR = 4.3$ , developing a span-wise Reynolds- $Re$ -number range from root to tip of  $1.7 \cdot 10^5 < Re < 3.0 \cdot 10^5$ . The axial inflow velocity is captured by two parallel Prandtl tubes that are permanently installed at approximately one rotor radius upstream, close to each wind tunnel wall and slightly above hub-height. At rated conditions, the inflow velocity is  $6.5 \text{ ms}^{-1}$  at a rotational frequency of  $f_{rot} = 3.0 \text{ Hz}$ . The Data Acquisition (DAQ) system of the rotating sensors, such as pressure taps and strain gauges, is installed within the rotational spinner, displayed in **Figure 6** (a). The electrical power is transferred to the rotating system through a slip ring. Communication with the host PC is established via WIFI connection in order to set and modify the rotational speed. The DAQ system signals are captured on all channels simultaneously at rate of 10 kHz generating around  $6.0 \cdot 10^5$  data points per measurement that-which are streamed to a host PC via network connection.

Formatiert: Schriftart: Kursiv

Formatiert: Schriftart: Kursiv

Kommentiert [D5]: RC2, # 5: comment on blockage ratio.

## 2.2. Blade configurations and operation points

The test matrix consists of four blade configurations, three operation points and three measurement methods, which are specified throughout this section.

Table 1. Blade configurations

	Tripped case	Clean case
Baseline	Operation points	
GF = 0.5 %c		
GF = 1.0 %c		

### 2.2.1 Forced transition

Following Klein et al. (2018), the principal baseline configuration of the BeRT includes Zig Zag (ZZ) turbulator tape, in short, the tripped case. ZZ tape is applied in order to initiate the laminar-to-turbulent transition of the Boundary Layer (BL) at a fixed location. In practical terms, it is used to emulate LE roughness effects on both airfoil sections (Rooij and Timmer, 2003) and as well as rotor blades (Zhang et al., 2017). Its height is slightly smaller than the local BL thickness,  $\delta_x$ , in order to trigger the BL transition while avoiding the a disproportionate drag increase or even turbulent separation. The ZZ tape is implemented on all BeRT blades at a chord-wise LE position of both the Suction Side (SuS) at  $x_{SuS} = 5.0$  %c and the Pressure Side (PrS) at  $x_{PrS} = 10.0$  %c. The BL thickness of the clean baseline,  $\delta_x$ , is calculated using with the software XFOIL, developed by (-Drela, (1989), based on the Re-number, the AoA and the N-criterion (Ncrit) modeling the transition location. The design conditions of the Clark-Y airfoil are defined by  $\alpha_{opt} = 5.0^\circ$ ,  $Re \approx 2.5 \cdot 10^5$  and  $N_{crit} = 6$  accounting for the elevated  $Ti$  inside the test section (Sect. 2.1). Hence as such, the attached flow at pre-stall conditions is assumed quasi-2D two-dimensional in order to estimate  $\delta$  by means of the XFOIL code. The absolute height of the ZZ tape is adjusted in various steps in relation to the chord-length, as depicted in Figure 4 (a). In addition, all experiments are also performed considering under the consideration of the free BL transition, i.e. without including ZZ tape, in short, the clean case, without including ZZ tape.

### 2.2.2 Gurney flaps

The GF-height is supposed to be submerged by-into the BL at the TE in order to keep the induced drag penalty on an acceptable level, as discussed in Sect.1. Hence, it is important to estimate  $\delta$  before dimensioning the GF-height, since the aerodynamic impact depends on the  $GF/\delta$  ratio. Apart from the AoA and the transition location,  $\delta$  is related to  $Re$ . The Re-number range of the BeRT is significantly lower compared to the blades of multi-MW HAWTs. Considering At design conditions ( $Re \approx 2.5 \cdot 10^5$ ), the XFOIL code predicts the BL thickness at the TE to be  $\delta_{TE} = 1.0$  %c. Furthermore Additionally, another GF-height of half the local  $\delta$  is chosen, so that the GF configurations include consist of  $GF = 1.0$  %c and  $GF = 0.5$

Formatiert: Standard

Kommentiert [D6]: RC2, # 8: split up and rearrange tables

Formatiert: Schriftart: Nicht Fett

Formatiert: Zentriert

Formatierte Tabelle

Formatiert: Zentriert

Formatiert: Zentriert

Formatiert: Zentriert

Formatiert: Englisch (Vereinigtes Königreich)

Formatiert: Standard

Formatiert: Standard

Formatiert: Schriftart: Kursiv

Kommentiert [D7]: RC2, #6: XFOIL = software

Kommentiert [D8]: RC2, # 7: explain relevance of BL estimation based on 2D flow

Formatiert: Schriftart: Kursiv

Kommentiert [D9]: RC1, # 4: specify statement on design considerations to limit drag penalty

Formatiert: Schriftart: Kursiv

Formatiert: Schriftart: Kursiv

Formatiert: Schriftart: Kursiv

145 %c. For comparison, the FFA-W3-241 airfoil ( $t/h_{max} = 24.1\%$ ,  $Re = 12 \cdot 10^6$ ,  $\alpha_{opt} = 10.0^\circ$ ), which is used in the outer blade region of the DTU 10MW RWT (Bak et al., 2013), develops a BL of  $\delta_{TE} \approx 0.30\%$ . As such, the application of  $GF > 0.30\%$  would be likely to cause the L/D ratio to decline, as illustrated in Figure 2 (b).

150 Apart from the very tip section, ~~they~~ the GFs are implemented in the form of thin angle profiles made of brass. One side of the angle profiles is cut in a linear way in order to match the chord decrease, as shown in Figure 4 (b). The other side of the profile is attached with thin double-sided adhesive tape adjacent to the TE.

**Formatiert:** Schriftart: Kursiv

**Formatiert:** Schriftart: Kursiv, Tiefgestellt

**Formatiert:** Tiefgestellt

**Formatiert:** Tiefgestellt

**Formatiert:** Schriftart: Nicht Kursiv

**Formatiert:** Schriftart: Kursiv

**Formatiert:** Schriftart: Nicht Kursiv

**Kommentiert [D10]:** RC2, # 9: clarify the statement  
Line 148-152 were rewritten and shifted to here

**Formatiert:** Schriftart: Nicht Kursiv

**Formatiert:** Schriftart: Nicht Kursiv

**Formatiert:** Schriftart: Nicht Kursiv

**Formatiert:** Schriftart: Nicht Kursiv

**Formatiert:** Schriftart: Nicht Kursiv

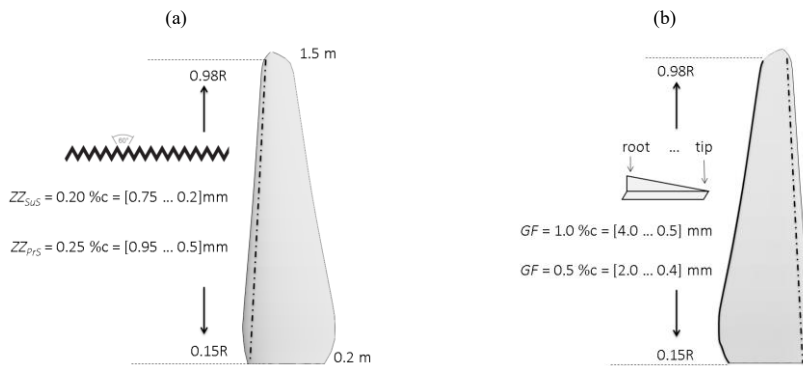


Figure 4. (a) Zig Zag tape at the leading edge of the suction side. (b) Gurney flap and ZZ tape at the pressure side of the trailing edge.

155 **2.2.3 Test matrix Operation points**

Table 1 summarizes the test matrix that consists of four blade configurations, three Operation Points (OPs) and three measurement methods. The Operation Points (OPs) include the so-called stall, rated and feather conditions, which are characterized by low, medium and high TSR or AoA, respectively, see Table 2. Each measurement has a total duration of 60 s. No blockage correction is applied, so that the results refer to the conditions inside the closed test section. All sensors are calibrated and a zero-offset measurement is performed before each test-run in order to reduce experimental errors. The uncertainty of the results is evaluated in Appendix B Appendix B.

160

Table 24. Summary of Test matrix operation points.

	Stall	Rated	Feather
TSR	3.0	4.3	5.6
Inflow velocity in $m s^{-1}$	6.5	6.5	5.0
Rot. frequency in Hz	2.1	3.0	3.0
Re-number (Sect. 3.2)	$2.2 \cdot 10^5$	$2.8 \cdot 10^5$	$2.7 \cdot 10^5$
AoA in $^\circ$ (tripped baseline, Sect. 3.1)	16.3	8.8	4.8
AoA in $^\circ$ (clean baseline, App. A)	16.5	8.6	4.6

165

Formatierte Tabelle

Kommentiert [D11]: RC2, #.8: rearrange tables

Kommentiert [D12]: RC2, #.8: split up and rearrange tables and include clean case

Formatierte Tabelle

Formatiert: Schriftart: Fett

Formatiert: Schriftart: Fett

Formatiert: Schriftart: Fett

Formatiert: Schriftart: Fett

Formatiert: Schriftart: Fett

Formatiert: Schriftart: Fett

Formatiert: Schriftart: Fett

Formatiert: Schriftart: Fett

Blade configuration		Operation point (clean case)						
	Tripped-baseline	Clean-baseline	Stall	Rated	Feather			
$GF=0.5\%c$	Operation points				TSR	3.0	4.3	5.6
$GF=1.0\%c$					Inflow velocity in $ms^{-1}$	6.5	6.5	5.0
Measurement method		Rot. frequency in Hz	2.1	3.0	3.0			
Ultrasonic anemometry	Wake velocities $\rightarrow$ AoA	AoA in $^{\circ}$ (Sect. 3.1)	16.5	8.6	4.6			
Pressure taps	$e_p$ -distribution $\rightarrow$ lift curve	Re-number (Sect. 3.2)	2.2-10 <sup>5</sup>	2.8-10 <sup>5</sup>	2.7-10 <sup>5</sup>			
Strain gauges	Root-bending moments							

Kommentiert [D13]: RC2, #.8: rearrange tables

The Re numbers, see Table 1, are determined by means of the experimental method that is laid out in Sect. 2.3. They are significantly lower compared to the Re numbers of several millions that occur along the blades of multi MW HAWTs. Nonetheless, the effectiveness of the Gurney flap is determined by the ratio between its height and the corresponding boundary layer thickness, especially in terms of the resulting L/D ratio, see Figure 2 (b). Hence, the present findings are considered relevant beyond the Re numbers of the BeRT blades, as long as the GF/BL ratio is kept constant.

Kommentiert [D14]: RC2, # 9: clarify the statement  
 → This paragraph was rewritten and shifted to Sect 2.2.2.

### 2.3 Measurement methods

The measurement methods listed in Table 1 consist of three types of sensors. The experimental approaches are summarized in Table 3 and explained in detail throughout this section, that are simultaneously recording the wake velocity, the pressure distribution and the root-bending moments.

Table 3. Measurement methods and quantities

Sensor	Measured quantity	Derived quantity	Blade position
Ultrasonic Anemometer	3D wake velocities	AoA	0.56R
Pressure taps	Pressure distribution	Lift coefficients	0.45R
Strain gauges	Flapwise and edgewise bending moments	Blade root	

Kommentiert [D15]: RC2, # 8: split up and rearrange tables  
 RC1, # 3: clarify blade-positions

Formatiert: Schriftart: Nicht Fett

Formatiert: Absatz-Standardschriftart

Formatiert: Beschriftung

Formatiert: Schriftart: Nicht Fett

Formatiert: Zentriert

Formatierte Tabelle

Formatiert: Schriftart: Fett

Formatiert: Schriftart: Fett

Formatiert: Schriftart: Fett

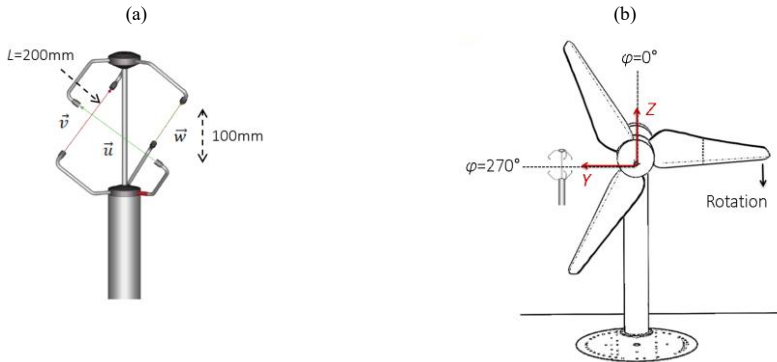
Formatiert: Zentriert

Formatiert: Zentriert

Formatiert: Zentriert

#### 2.3.1 Ultrasonic anemometry

3D Ultrasonic Anemometers (UAs) are widely spread in the wind energy industry. The technology is recognized by different wind industry standards such as the IEC 61400 to determine the power curve of wind turbines or the Association of German Engineers (VDI) for turbulence measurements. Moreover, there are numerous references for the use of UAs in the context of wind tunnel campaigns, such as Weber et al. (1995), Hand et al. (2001) and Cuerva et al. (2003). The UA is a commercial product of Thies CLIMA (version 4.383). According to the manufacturer, they are pre-calibrated and free from maintenance.



185 **Figure 5.** (a) Ultrasonic Anemometer, reproduced and modified from Thies CLIMA. (b) Definition of the azimuthal blade positions looking downstream.

**Figure 5** (a) displays the three separate acoustic transmitter-receiver pairs that are installed orthogonally to each other. The velocity vectors,  $\vec{u}$ ,  $\vec{v}$  and  $\vec{w}$ , are determined by six individual measurements based on the bidirectional time-of-flight principle, i.e. the duration of each signal to be sent and received,

190

$$\vec{u} = \frac{L}{2} \left( \frac{1}{t_1} - \frac{1}{t_2} \right), \quad (1)$$

where  $L = 200 \text{ mm}$  is the exact running-length between each sensor pair, so that the measurement volume amounts to  $(100 \times 200 \times 200) \text{ mm}^3$ . The velocity vectors  $\vec{v}$  and  $\vec{w}$  are determined accordingly. Eq. (1) shows that the 3D velocity calculation depends solely on the average propagation time of the ultrasound,  $t_1$  and  $t_2$ , depending on the specific airflow passing through the measurement volume. As such, the output values already imply the density and temperature of the air. Subsequently, the velocity vectors are transformed into a natural coordinate system, so that the output time-series consist of the axial, lateral and

195

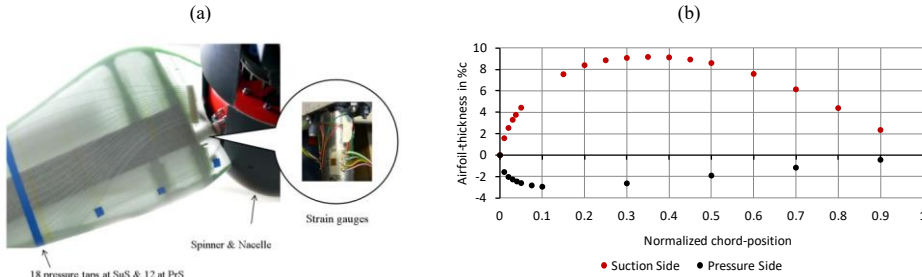
vertical velocity components,  $u$ ,  $v$  and  $w$ . The device-internal [data acquisition DAQ](#)-system is a half-duplex interface that is completely independent of both the wind tunnel and the BeRT system. According to the manufacturer, the measurement accuracy is  $0.1 \text{ m}_s^{-1}$  per integrated value and  $0.01 \text{ m}_s^{-1}$  with respect to each of the three velocity components. The data is recorded at a sampling rate of 60 Hz thus providing around 3600 data points per measurement. Considering the relatively large measurement volume and the low sampling rate compared to e.g. hotwire or laser-based devices, the UA is not adequate for the investigation of complex or high-speed flow structures. However, the BeRT wake-flow is expected to consist of an axial and a tangential velocity component due to the formation of a rotating wake tube. The impact of complex tip and root vortices is considered negligible in the mid-span blade region, as shown by Herráez et al. (2018).

200

205 The UA is installed at one static position downstream,  $X = 1.3R$ , in the mid-span region,  $Y = 0.56R$ , and at hub height,  $Z = 0R$ , see [Figure 5](#) (b). It is positioned vertically with a spirit level and turned around its own axis towards the undisturbed axial inflow, so that the lateral and the vertical components,  $v$  and  $w$ , tend to zero. The set-up is fixed at its final position for all measurements, which are presented in Sect. 3.

### 2.3.2 Pressure taps

210 The pressure distribution is extracted by means of 18 Pressure Taps (PTs) on the SuS and 12 on the PrS, located along the chord-length at  $r = 0.45R$ , see [Figure 6](#) (b). Each orifice is connected via silicone tubing to its corresponding differential pressure sensor (HCL0025E), i.e. the pressure box inside the spinner. The sensor accuracy is given with 0.05 % of the full scale range of  $\pm 2500$  Pa under nominal conditions. The experimental procedure and the data post-processing is based on Soto-Valle et al. (2019).



215 **Figure 6.** (a) BeRT blade and pressure taps, reproduced and modified from Fischer (2015). (b) Chord-wise position of pressure taps at  $r = 0.45R$ .

The differential pressure values are transformed into the pressure coefficient,

$$c_{pi} = \frac{\Delta p_{sti} + p_{rot}}{p_{dyn,ref}} = \frac{(p_{sti} - p_{st,\infty}) + (0.5\rho \cdot (\omega r)^2)}{p_{dyn,ref}}, \quad (2)$$

220 where

- $\Delta p_{sti}$  is the static pressure difference between each PT and the inflow Prandtl tube  $p_{st,\infty}$ .
- $p_{rot}$  refers to the pressure due to the rotation of the blade element. It is added to  $\Delta p_{sti}$  in the form of a constant correction term in accordance with Hand et al. (2001).
- $p_{dyn,ref}$  describes the referential dynamic pressure, i.e. the effective flow velocity experienced by the blade element.

225 Following Hand et al. (2001), it is determined by the maximum pressure that is recorded on the pressure side, the



frontal stagnation point, where  $c_{pi} = 1.0$ . According to Eq. (2)(2) the referential dynamic pressure is then determined calculated with by  $p_{dyn,ref} = \Delta p_{st,ref} + p_{rot}$ .

The  $c_p$  values are phase-averaged over an azimuthal angle of  $\varphi = 10^\circ$ , see (Figure 5 Figure 5 (b)). Each PT provides a total of 36 pressure values at the following blade positions:  $\varphi = [0^\circ, 10^\circ, 20^\circ \dots 350^\circ]$ , so that  $\varphi = 270^\circ$  contains the average of all data points between  $265^\circ < \varphi < 275^\circ$ . The pressure difference,  $\Delta c_p$ , is calculated by subtracting the integrated  $c_p$  distribution between the PrS and the SuS in order to determine both the normal coefficient,  $c_n$ , and the tangential coefficient,  $c_t$ . Per definition,  $\vec{c}_n$  is orthogonal to the chord-line pointing towards the SuS, while  $\vec{c}_t$  is parallel to the chord-line pointing towards the LE.

According to Hand et al. (2001), the axial and tangential coefficients are calculated with

$$c_n = \frac{1}{2} \cdot \sum_{i=1}^{30} (c_{pi} + c_{pi+1}) \cdot (x_{i+1} - x_i) \quad (3)$$

and

$$c_t = \frac{1}{2} \cdot \sum_{i=1}^{30} (c_{pi} + c_{pi+1}) \cdot (y_{i+1} - y_i), \quad (4)$$

where  $x$  and  $y$  are the normalized chord positions of each PT. The numbering starts at the TE ( $x = 0.9$ ) with the 18-PTs on the SuS<sub>1</sub> moving anti-clock wise until the LE ( $x = 0$ ) and back to the TE on the PrS.

Subsequently, the lift coefficient,  $c_l$ , and the pressure drag coefficient,  $c_{dp}$ , is are determined by (Fuglsang et al., 1998)

$$c_l = c_n \cdot \cos(\alpha) + c_t \cdot \sin(\alpha); \quad (5)$$

and

$$c_{dp} = c_n \cdot \sin(\alpha) - c_t \cdot \cos(\alpha). \quad (6)$$

The required AoA,  $\alpha$ , are adopted by the uncorrected inflow and wake velocity measurements (Sect. 3.1). At pre-stall conditions, i.e. considering small AoA,  $c_t \ll c_n$ , so that  $c_n \approx c_l$  (Barlow et al., 1999). It is noted that Eq. (6) describes the pressure drag which does not account for the skin-friction drag component. Hence, it is not possible to extract the total drag,  $c_d$ , of the blade element via the local  $c_p$  distribution (Houghton et al., 2013).

The term  $c_t \cdot \sin(\alpha)$  in Eq. (5) solely describes the pressure drag, which does not contain the skin-friction drag, so that  $c_t \cdot \sin(\alpha) \ll c_d$ . Moreover, for relatively small AoA,  $c_t \ll c_n$  (Barlow, 1999).

Formatiert: Schriftart: Kursiv

Formatiert: Schriftart: Kursiv

Formatiert: Schriftart: Nicht Fett

Formatiert: Beschriftung, Vom nächsten Absatz trennen

Formatierte Tabelle

Formatiert: Schriftart: Nicht Kursiv

Formatiert: Schriftart: Nicht Kursiv

Feldfunktion geändert

Formatiert: Schriftart: Nicht Fett

Kommentiert [D16]: RC1, #.5: include lift over drag performance

Formatiert: Schriftart: Kursiv

Formatiert: Schriftart: Kursiv, Tiefgestellt

Formatiert: Schriftart: Kursiv

Formatiert: Schriftart: Kursiv, Tiefgestellt

### 2.3.3 Strain gauges

The Strain Gauges (SGs) are mounted at the clamping of the blade (Figure 6 (a)) detecting the Root Bending Moments (RBMs) in the out-of-plane or flapwise and in-plane or edgewise direction, see Figure 6 (a). They are connected in a full-bridge configuration aiming at the mitigation of temperature and cross talk effects (FAET-A6194N-35). The experimental procedure to determine the RBMs is based on Bartholomay et al. (2018). For the purpose of the presented baseline measurements, a simplified post-processing protocol is applied without including the data-based cross talk correction.

Before testing each blade configuration, the offset signal is recorded in slow-motion at the lowest rotating frequency available,  $f_{rot} = 0.1$  Hz. In this way, the gravitational RBMs are subtracted from the results, which are otherwise registered as a sinusoidal signal in the edgewise direction. At operational frequencies, the axial forces due to the blade rotation are causing a material deformation directed towards the blade tip. They are quantified as a combination of centrifugal and gravitational forces by

$$F_{axial} = F_{cent} - F_{grav} = (m_{blade} \cdot r_{cg} \cdot \omega^2) - (m_{blade} \cdot g \cdot \cos(\varphi)), \quad (76)$$

where  $m_{blade} = 5.67$  kg, the center of gravity is located at  $r_{cg} = 0.31R$ ,  $g$  is the gravitational constant and  $\varphi$  refers to each phase-locked blade position. The rotational frequency,  $\omega$ , is kept constant during each test-run so that the centrifugal force  $F_{cent}$  becomes a constant correction term at each OP. The effective flapwise and edgewise RBMs, which are related exclusively to the aerodynamic loads acting on the blade, are determined by

$$M_{flap}(\varphi) = (U_{f,raw}(\varphi) - U_{f,off}(\varphi)) \cdot K_{f1} - (F_{axial} \cdot K_{f2}) \quad (87)$$

and

$$M_{edge}(\varphi) = (U_{e,raw}(\varphi) - U_{e,off}(\varphi)) \cdot K_{e1} - (F_{axial} \cdot K_{e2}), \quad (98)$$

where

- $M_{flap}$  and  $M_{edge}$  are the aerodynamic flapwise or edgewise RBMs in Nm.
- $U_{f,raw}$  and  $U_{e,raw}$  stand for the raw data signal in V.
- $U_{f,off}$  and  $U_{e,off}$  describe the slow-motion offset signal in V.
- $K_{f1}$  and  $K_{e1}$  refer to constant calibration factors to transform V into Nm.
- $K_{f2}$  and  $K_{e2}$  refer to constant calibration factors to transform the axial forces from N into Nm.

Applying Eq. (87) and (98) both the out-of-plane and the in-plane RBMs are computed for each of the 36 blade positions, see Sect. 3.

Kommentiert [D17]: RC2, #10: typo

### 3 Results

The measurement results of both the tripped and the clean cases are presented and discussed. For space economy, the clean case is only included in terms of the concluding results, such as the lift performance in Sect. 3.2 and the root bending moments in Sect. 3.3, but otherwise accessible in Appendix A for completeness.

#### 3.1 Wake velocities and angles-of-attack

Following Snel et al. (2009), Figure 7(a) shows the average axial and tangential wake velocity normalized by the axial inflow velocity at each OP,  $uu_{\infty}^{-1}$  and  $wu_{\infty}^{-1}$ .

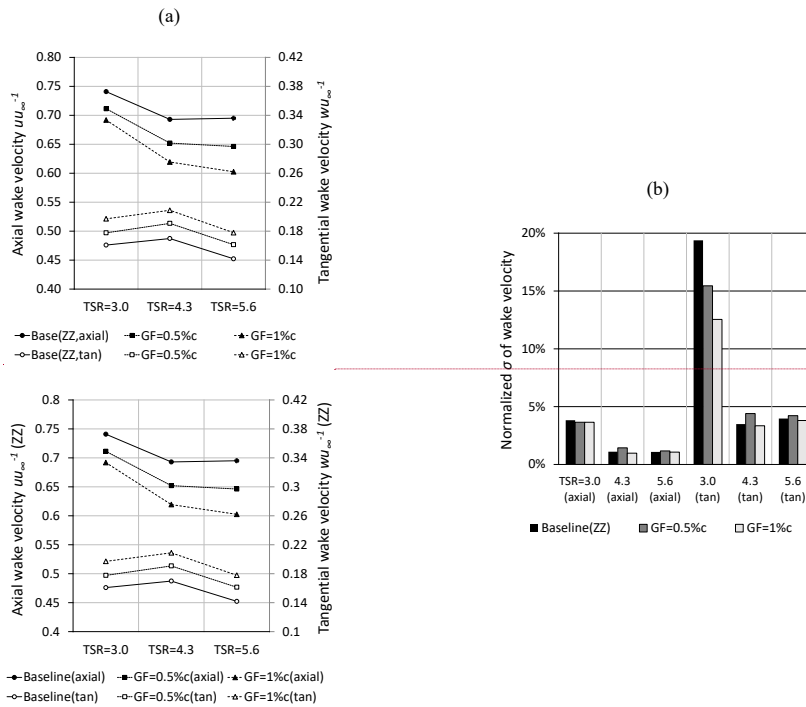


**Figure 7.** Tripped case at  $r = 0.56R$  and  $\varphi = 270^\circ$ . (a) Mean axial and tangential (tan) wake velocity normalized by the inflow velocity. (b) Standard deviation of the wake velocity normalized by the average wake velocity.

Starting from the baseline, Figure 7 (a) shows that the axial wake velocities are found to be significantly higher compared to typical typical-free flow conditions -without wind tunnel walls. Figure 7 (a). According to the steady state Blade Element

Formatierte Tabelle

Kommentiert [D18]: RC2, # 11: clarify which curves belong to axial and to tangential velocity

Kommentiert [D19]: RC2, #12: specify the meaning of free flow conditions

Momentum (BEM) method, the optimum axial wake velocity is supposed to be around one third of the inflow (Burton *et al.*, 2011). In this case, it amounts to more than two thirds at all OPs. This phenomenon is caused by the wind tunnel blockage effects, previously shown by CFD simulations using the fluid dynamic code FLOWer. At rated conditions of the BeRT, Klein *et al.* (2018) conclude that the flow decelerates to an axial wake velocity in the range of  $0.62u_\infty < u_{CFD} < 0.77u_\infty$ , which is in agreement with the experimental results,  $u_{exp} = 0.69u_\infty$ . The Furthermore, the corresponding tangential velocity, on the other hand, is similar to the steady state BEM simulation of QBlade (Marten *et al.*, 2013) with  $w_{BEM} = 0.18u_\infty$  compared to  $w_{exp} = 0.17u_\infty$  (Marten *et al.*, 2013). Hence, the tangential wake velocity is relatively close to the standard BEM simulation, despite the influence of the wind tunnel walls. According to Eq. (11),  $w$  depends primarily on the rotational speed of the blade. As such, the tangential wake velocity is less affected by the wind tunnel blockage effect.

Regarding the impact of the GFs, Figure 7 (a) illustrates the consistent decrease of the axial, and the consistent increase of the tangential wake velocity both in relation to the GF-height. The lateral velocity component is neglected as it amounts to  $v \ll |\pm 0.1 \text{ ms}^{-1}|$ . Figure 7 (b) summarizes shows the standard deviation normalized by the corresponding average velocity component, as such describing the 1D turbulence intensity, expressed in percent (Burton *et al.*, 2011). As expected, the flow separation,  $TSR = 3.0$ , is captured by the UA in the form of a more turbulent wake field, especially regarding the tangential component. The GF configurations do not influence the wake turbulence considerably, except for the tangential velocity component at stall,  $TSR = 3.0$ , where the GFs appear to mitigate the turbulence level.

Next According to the BEM method (Hansen, 2015), the wake velocity is converted into the axial and tangential rotor induction factors,

$$a = \frac{1}{2} \left( 1 - \frac{u}{u_\infty} \right) \quad (109)$$

and

$$a' = \frac{w}{2\omega r} \quad (110)$$

The induction factors,  $a$  and  $a'$ , describe the decrease of the axial, and the increase of the tangential velocity component from a reference point sufficiently far away from the rotor plane rather than the rotor plane itself (Burton *et al.*, 2011). The wake measurements are taken recorded at a distance of  $X = 1.3R$  downstream in order to avoid the influence of the wind tunnel contraction, see Figure 3 (a).

Subsequently, According to Hansen (2015) and Eq. (9) and (10), the AoA is are derived from by means of Eq. (10) and (11) with

**Kommentiert [D20]:** RC2, # 13: comment on tangential velocity and blockage effects

**Formatiert:** Schriftart: Nicht Kursiv

**Formatiert:** Schriftart: Kursiv

**Formatiert:** Englisch (Vereinigtes Königreich)

$$\alpha = \arctan\left(\frac{(1-a)u_\infty}{(1+a')\omega r}\right) - \beta = \arctan\left(\frac{u_\infty + u}{2\omega r + w}\right) - \beta, \quad (1244)$$

where the twist-angle at the radial location of the UA is  $\beta(0.56R) = 9.8^\circ$ .

325

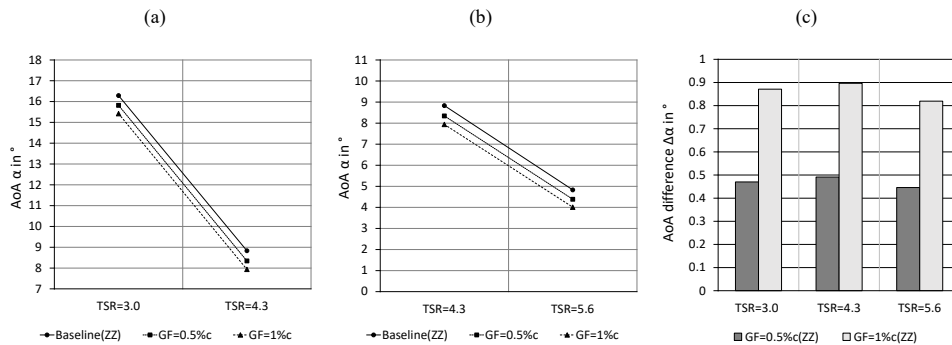


**Figure 8.** Angles-of-attack in the tripped case at  $r = 0.56R$  and  $\varphi = 270^\circ$ . (a) Stall and rated conditions (b) Rated and feather conditions (c) AoA difference between Gurney flap configurations and the baseline.

At rated conditions, the AoA of the baseline case is  $\alpha_{ZZ} = 8.8^\circ$ , see [Figure 8](#) (a) and (b). This outcome is in general agreement with previous different experimental and numerical investigations of the BeRT, gathered in [Table 4](#), based on 3-hole probes as well as CFD simulations of the BeRT, detailed by [Klein et al. \(2018\)](#). Hence, the AoA are considered stable with respect to the mid-span region, i.e.  $0.65R < r < 0.45R$ .

[Table 4.](#) Comparison of approximate AoA results at rated conditions and  $\varphi = 270^\circ$ .

Method	Blade position	Case	AoA	Reference
Pressure taps	0.45R	clean	8.0°	Soto-Valle et al. (2020)
Ultrasonic Anemometry	0.56R	tripped	8.8°	Present study
3-hole probe	0.65R	tripped	8.5°	Klein et al. (2018)
CFD simulation	0.65R	tripped	8.2°	Klein et al. (2018)

The different experiments ([Table 4](#)) result in local AoA that are significantly higher compared to the original blade design of the BeRT,  $\alpha_{opt} = 5.0^\circ$ . Due to the built-in twist angles, the AoA is considered constant in the mid-span region, i.e. within the range of  $0.45R \leq r \leq 0.65R$ .

Furthermore, [Figure 8](#) (c) displays the consistent AoA decrease caused by the GF configurations. Depending on the GF height, the AoA differences between GF and Baseline configurations amounts to  $\Delta\alpha_{GF=0.5\%c} = 0.5^\circ$  and  $\Delta\alpha_{GF=1.0\%c} = 0.9^\circ$ , i.e. to a level that is closer to the optimum blade operation, more favorable level in terms of the BeRT rotor. Hence, as such, the results quantify an important effect of retrofitted-GFs on the blade performance; decreasing axial wake velocities and thus reduced AoA.

Formatiert: Schriftart: Kursiv

Kommentiert [D21]: RC1, # 3: specify blade positions of measurements and clarify the assumption of stable AoA throughout the mid span region

Formatiert: Schriftart: Nicht Fett

Formatiert: Beschriftung

Formatiert: Schriftart: Nicht Fett

Formatiert: Schriftart: Nicht Fett

Formatiert: Schriftart: Nicht Fett

Formatiert: Schriftart: Fett

Formatiert: Zentriert

Formatiert: Schriftart: Fett

Formatiert: Schriftart: Fett

Formatiert: Zentriert

Formatiert: Zentriert

Formatiert: Zentriert

Formatiert: Zentriert

Formatiert: Zentriert

Formatiert: Zentriert

Formatiert: Zentriert

Formatiert: Zentriert

Formatiert: Zentriert

Formatiert: Schriftart: Nicht Kursiv

Kommentiert [D22]: RC2, #16: comment on different blade positions of AoA and cl calculations

Kommentiert [D23]: RC1: typo

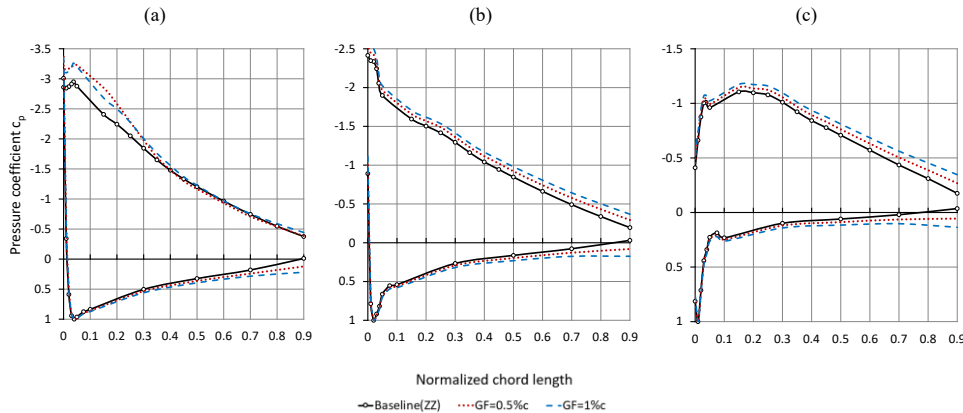
Kommentiert [D24]: RC2, #14: define  $\Delta\alpha$

Kommentiert [D25]: RC2, # 15: rephrase this statement for clarity

345 In the following Sect. 3.2, the AoA are correlated ~~to~~ with the normal force coefficients  ~~$c_n$~~   $c_n$  in order to obtain the lift coefficients  ~~$c_l$~~   $c_l$ .

### 3.2 Pressure distribution and lift performance

Figure 9 shows the distribution of the pressure coefficients,  $c_p$ , ~~regarding in relation to~~ the different OPs.



350 **Figure 10.** Pressure ~~distribution-coefficients~~ in the tripped case with respect to different scales at  $r = 0.45R$  and  $\varphi = 270^\circ$ . (a)  $TSR = 3.0$ . (b)  $TSR = 4.3$ . (c)  $TSR = 5.6$ .

355 The  $c_p$  curves shown in Figure 10 (b) and (c) represent the pre-stall cases at  $\alpha_{TSR=4.3} = 8.8^\circ$  and  $\alpha_{TSR=5.6} = 4.8^\circ$ , respectively. At stall,  ~~$TSR = 3.0$ , see Figure 10 (a), the separation at the SuS is not yet complete, despite the elevated AoA,  $\alpha_{TSR=3.0} = 16.3^\circ$ . The curves  $\alpha_{ZZ} = 16.3^\circ$ . Compared to XFOIL simulations (Sect. 2.3.1), the maximum lift coefficient of the Clark Y airfoil is already reached at  $c_{l,max} \sim 14.0^\circ$ . Hence, the  $c_p$  curves seen in Figure 10 (a) indicate the effect of stall delay due to the blade rotation, as discussed hereafter.~~

360 Moreover, the GF configurations cause an expansion of the pressure differences between the PrS and the SuS,  $\Delta c_p$ , along the complete chord-length and regarding all OPs. This effect is particularly visible in terms of the aft-loading towards the TE at  $0.5 < x < 0.9$ . As such,  $\Delta c_p$  reflects the increased circulation due to the GF applications, as reported by Storms and Jang (1994) based on the clean NACA 4412 airfoil ( $h_{max} = 12.0\%$ ,  $Re = 2.0 \cdot 10^6$ ).

- Formatiert: Tiefgestellt
- Formatiert: Schriftart: Nicht Kursiv
- Formatiert: Schriftart: Nicht Kursiv
- Formatiert: Schriftart: Nicht Kursiv
- Formatiert: Schriftart: Nicht Kursiv

- Kommentiert [D26]: RC2, # 17 and 18: rewrite the whole paragraph for more clarity
- Formatiert: Schriftart: Kursiv
- Formatiert: Tiefgestellt
- Formatiert: Englisch (Vereinigtes Königreich)

In order to quantify the results, the  $c_p$  distribution is transformed into the local lift curve based on Eq. (5.5). The required AoA are adopted from Sect. 3.1, so that the lift coefficients combine the results of both the wake-velocity and the pressure measurements.

365



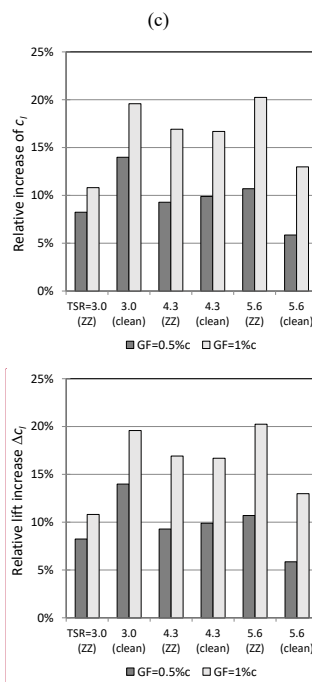
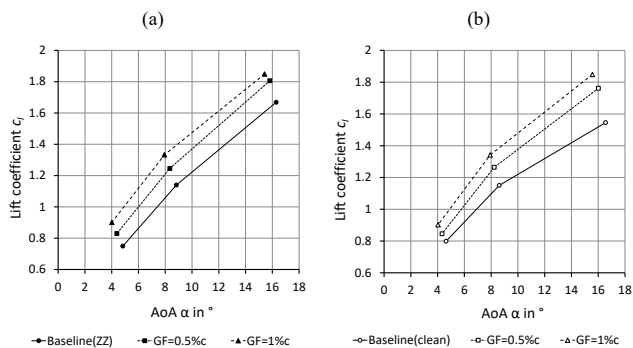


Figure 11. Lift coefficients over angles-of-attack at  $r = 0.45R$  and  $\varphi = 270^\circ$ . (a) Tripped case. (b) Clean case. (c) Relative lift increase of Gurney flap configurations in relation to the corresponding baseline.

Figure 11(a) and (b) depict the lift coefficients of both the tripped and the clean cases. Starting from the baseline, the tripped case shows smaller  $c_l$  at  $4^\circ < \alpha < 5^\circ$  because of the forced BL transition at the LE. At  $8^\circ < \alpha < 9^\circ$ , this is not the case anymore, while in the stall region,  $15^\circ < \alpha < 17^\circ$ , the ZZ tape appears to develop a beneficial effect on the lift performance. This phenomenon is probably caused by the tripped and more turbulent BL that remains attached until closer to the TE. In the clean case, however, the less energetic BL separates earlier thus leading to smaller  $c_l$  at elevated AoA. This observation is confirmed by comparable airfoil experiments on the FX 63-137 airfoil section at  $(\mu)_{max} = 13.7\%c$ ,  $Re = 1.0 \cdot 10^5 < Re < 2.0 \cdot 10^5$  using ZZ tape with a thickness of 0.75 mm (Holst et al., 2016). Despite the decrease in the pre-stall, the lift coefficients are found on a similar level in the post-stall region.

Kommentiert [D27]: The naming of the y-axis was changed ( $c_l > \Delta c_l$ )

Formatiert: Schriftart: Kursiv

Formatiert: Schriftart: Kursiv, Tiefgestellt

Formatiert: Tiefgestellt

380 Furthermore, looking at the GF configurations (Figure 11 (a) and (b)), the lift  $c_l$  performance in the tripped case is on a similar, or even higher level considering the complete AoA range,  $4^\circ < \alpha < 17^\circ$ . Hence, forced LE transition ~~is does not neutralize or mitigate mitigating or neutralizing~~ the GF effect. In fact, the GF configurations appear to alleviate the adverse effects of LE roughness by improving the local lift  $c_l$  performance. Figure 11 (c) summarizes highlights the relative ~~er lift increase,  $\Delta c_l$ , of both between the GF configurations in relation to and~~ the corresponding baseline configuration ~~seases~~. At rated conditions,  $TSR = 4.3$ ,  $\Delta c_{l,GF=0.5\%c} = 0.11$  or 9.3 % and  $\Delta c_{l,GF=1.0\%c} = 0.19$  or 16.9 %, illustrating the main characteristic of retrofit GFs; the considerable lift increase.

390 Moreover, [the scale-level of both  $c_l$  and  $\Delta c_{l,GF=1.0\%c}$ ] is in agreement with comparable wind tunnel experiments based on a similar Clark-Y airfoil section, as depicted in Figure 12.

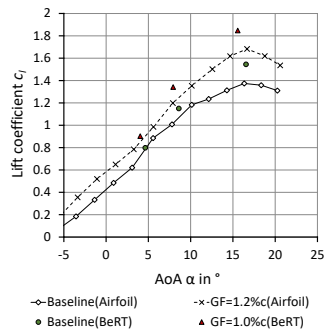


Figure 12. Lift coefficients of a Clark-Y airfoil including Gurney flap, reproduced and modified from Kheir-Aldeen (2014).

395 Figure 12 compares the lift coefficients of the clean Clark-Y airfoil section ( $th_{max} = 14.0\%$ ,  $Re = 2.1 \cdot 10^5$ ,  $GF = 1.2\%$ ) and the clean Clark-Y blade element of the BeRT ( $th_{max} = 11.9\%$ ,  $Re = 2.5 \cdot 10^5$ ,  $GF = 1.0\%$ ). The results demonstrate similarities for both the baseline and the GF configurations. The elevated  $c_l$  in case of the BeRT are due to the thinner Clark-Y blade element. At  $c_{l,max}$ , the blade performance is furthermore characterized by the radial flow due to the blade rotation causing stall delay. This behavior is in agreement with experiments on the field rotor at the Delft University of Technology. Rooij and Timmer (2003) report a significant shift of  $c_{l,max}$  compared to 2D airfoil simulations.

400 For completeness, the lift over the pressure drag coefficients (Eq. (6)) are displayed as an indicator of the drag performance.

It is reiterated that  $c_{dp} < c_{dl}$ , as previously discussed in Sect. 2.3.2.

(a)

(b)

(c)

Formatiert: Schriftart: Kursiv  
Formatiert: Schriftart: Kursiv, Tiefgestellt

Formatiert: Schriftart: Kursiv  
Formatiert: Schriftart: Kursiv, Tiefgestellt  
Formatiert: Schriftart: Kursiv

Kommentiert [D28]: RC2 # 19: specify the meaning of  $\Delta c_l$   
Formatiert: Schriftart: Kursiv  
Formatiert: Schriftart: Kursiv, Tiefgestellt

Formatiert: Schriftart: Nicht Fett  
Formatiert: Schriftart: Kursiv  
Formatiert: Schriftart: Kursiv, Tiefgestellt  
Formatiert: Englisch (Vereinigtes Königreich)  
Formatierte Tabelle

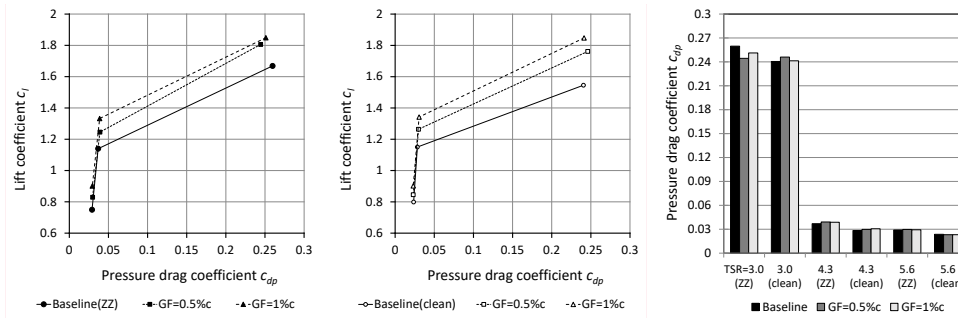


**Figure 13.** Lift over pressure drag coefficients at  $r = 0.45R$  and  $\phi = 270^\circ$ . (a) Tripped case. (b) Clean case. (c) Pressure drag coefficients in relation to the corresponding baseline.

405 **Figure 13 (a) and (b) illustrate the dependency of  $c_{dp}$  on the OP, reaching values of  $0.024 < c_{dp,pre-stall} < 0.04$  and  $c_{dp,stalk} \approx 0.25$ . In general, the baseline results are comparable to the clean S809 airfoil ( $th_{max} = 21.0 \%c$ ,  $Re = 3.0 \cdot 10^5$ ) that is used for the NREL Phase VI test turbine (Hand et al., 2001). Figure 13 (c) visualizes the increase of  $c_{dp}$  in the tripped case due to the implementation of the ZZ tape. The GF configurations, on the other hand, influence the  $c_{dp}$  values in a less noticeable way.**

410 After evaluating one area of the mid-span blade region, the impact of GFs over the complete blade span is presented in Sect. 3.3

### 3.3 Root bending moments

415 The integration of the aerodynamic loads, i.e. the lift and the drag forces acting along the blade span, yield the RBMs. The in-plane or edgewise RBMs are proportional to the rotor torque and thus the mechanical power output. They are directly related to the out-of-plane or flapwise RBMs, which are proportional to the rotor thrust and thus the structural loads (Hansen, 2015).

(a)

(b)

(c)

- Formatiert: Schriftart: Kursiv
- Formatiert: Schriftart: Kursiv, Tiefgestellt
- Formatiert: Schriftart: Kursiv
- Formatiert: Schriftart: Kursiv, Tiefgestellt
- Formatiert: Tiefgestellt
- Formatiert: Schriftart: Kursiv
- Formatiert: Schriftart: Kursiv, Tiefgestellt
- Formatiert: Tiefgestellt
- Kommentiert [D29]: RCI: # 5: include lift over pressure-drag plots

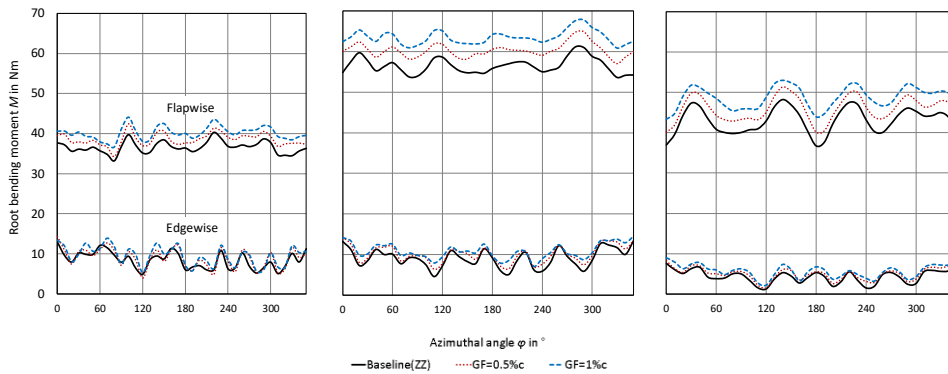
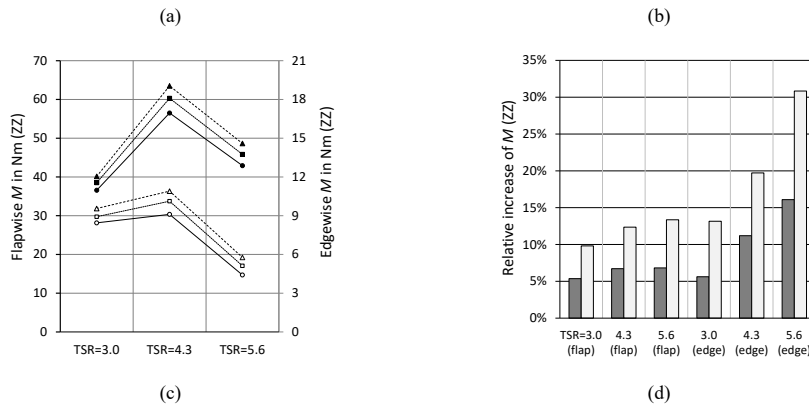


**Figure 14** Flapwise and edgewise root bending moments in the tripped case. (a)  $TSR = 3.0$ . (b)  $TSR = 4.3$ . (c)  $TSR = 5.6$ .

Figure 14 displays the aerodynamic RBMs that are recorded over one blade revolution in the form of 36 phase-locked blade positions. The impact of the GF configurations is registered as an overall increase of both the flapwise and the edgewise RBMs. In order to quantify and to discuss the results, the RBMs are presented as average values for both the tripped and the clean cases.



Formatierte Tabelle

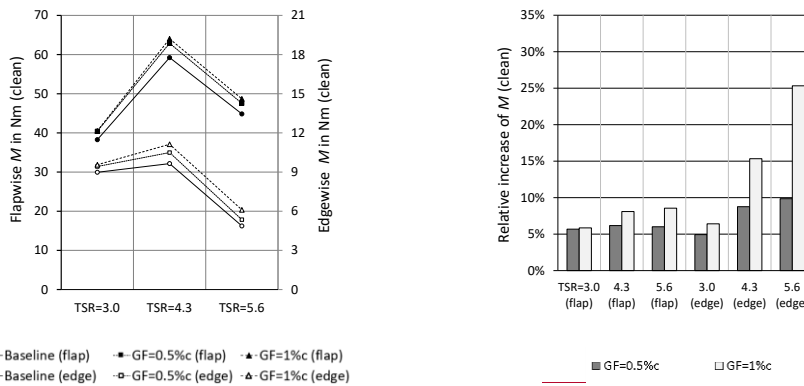


**Figure 154.** Flapwise (flap) and edgewise (edge) root bending moments. (a) Tripped case. (b) Relative increase to tripped baseline. (c) Clean case. (d) Relative increase to clean baseline.

The results of [Figure 15Figure 14](#) (a) confirm the increment of the average RBMs in relation to the GF-height in accordance with the previous [Figure 14Figure 13](#). In the clean case, the overall trend is similar to the tripped case considering all OPs, see [Figure 15Figure 14](#) (c). This means that the impact of the Gurney flaps, previously quantified in terms of the local lift coefficients, is now registered in the form of increased RBMs in both the flapwise and the edgewise direction.

In [Figure 15Figure 14](#) (b), the performance of the GF configurations is quantified in relation to the tripped baseline. At rated conditions, the average increase of the flapwise RBMs amount to  $\Delta M_{\text{flap,GF=0.5\%c}} = 3.8 \text{ Nm}$  or 6.7 % and to  $\Delta M_{\text{flap,GF=1.0\%c}} = 7.0 \text{ Nm}$  or 12.4 %. At the same time, the edgewise RBMs are enhanced by  $\Delta M_{\text{edge,GF=0.5\%c}} = 1.0 \text{ Nm}$  or 11.2 % and  $\Delta M_{\text{edge,GF=1.0\%c}} = 1.8 \text{ Nm}$  or 19.7 %. In the clean case, see [Figure 15Figure 14](#) (d), the overall trend is similar, however less pronounced. In both cases, the GF configurations generate performance improvements regarding the rotor torque, however albeit at the expense of the inherent increase of the rotor thrust.

FurthermoreOverall, the results reinforce the observation that GFs are more effective in relation to the tripped compared to the clean baseline. Looking at the relative increase shown in [Figure 15Figure 14](#) (b) and (d), the GF configurations appear to alleviate the effects of forced LE transition, especially on the edgewise RBMs, as previously discussed in Sect. 3.2 with respect to the local lift performance.

Formatiert: Schriftfarbe: Text 1

#### 440 4 Conclusions

The aerodynamic impact of Gurney flaps is investigated on the rotor blades of the Berlin Research Turbine. The test matrix consists of four blade configurations including the clean and the tripped baseline cases, as well as two GF configurations of 0.5% $c$  and 1.0 % $c$ . Furthermore, three measurement methods are applied, including 3D Ultrasonic Anemometry, surface pressure taps and strain gauges.

445 The baseline measurements confirm the influence of the prevailing wind tunnel blockage. At rated conditions,  $TSR = 4.3$ , and in the mid-span blade region, the axial wake velocity is approximately double in comparison to ideal free flow conditions, i.e. without wind tunnel walls. As such, the corresponding angles-of-attack are is elevated in comparison to the optimum blade design ease and amounts to  $\alpha_{exp} - \alpha_{exp} = 8.8^\circ$  rather than  $\alpha_{opt} = 5.0^\circ$ .

450 Under these circumstances, the retrofit application of Gurney flaps leads to performance improvements of both the tripped and the clean cases including tip speed ratios of 3.0, 4.3 and 5.6.

The impact of the Gurney flaps is registered regarding all blade configurations and operation points. In the tripped case and  $A_{at}$  rated conditions,  $TSR = 4.3$ , the axial wake velocities are reduced and the angles-of-attack are decreased by  $\Delta\alpha_{GF=0.5\%c} = 0.5^\circ$  and  $\Delta\alpha_{GF=1.0\%c} = 0.9^\circ$ . At the same time, the local lift coefficients are enhanced by  $\Delta c_{l,GF=0.5\%c} = 0.11$  or 9.3 % and  $\Delta c_{l,GF=1.0\%c} = 0.19$  or 16.9 %, which is the main characteristic of Gurney flaps. The effect of the aerodynamic loads over the complete blade span is analyzed by means of the root bending moments. The average increase in the out-of-plane direction amounts to  $\Delta M_{flap,GF=0.5\%c} = 3.8$  Nm or 6.7 % and to  $\Delta M_{flap,GF=1.0\%c} = 7.0$  Nm or 12.4 %. Simultaneously, the in-plane bending moments are augmented-elevated by  $\Delta M_{edge,GF=0.5\%c} = 1.0$  Nm or 11.2 % and  $\Delta M_{edge,GF=1.0\%c} = 1.8$  Nm or 19.7 %. Hence, decreasing angles-of-attack and increasing lift coefficients appear to be correlated with the enhancement of both the rotor torque and the thrust. Furthermore Overall, the aerodynamic impact of Gurney flaps effect is found more pronounced in the tripped case compared to the clean case.

465 The experimental results demonstrate the potential of retrofit Gurney flaps to improve the rotor blade performance in the following ways:

- Decreasing angles-of-attack to a level that is closer to the optimum blade operation.
- Elevated lift forces compensating for the adverse effects of forced leading edge transition.

470 In summary, Gurney flaps are considered a passive flow-control device worth investigating for the use on horizontal axis wind turbines of different sizes. However, the design of the Gurney flap-height in relation to the local boundary layer thickness is crucial in order to achieve performance improvements while avoiding detrimental effects such as indeed-additional drag

**Kommentiert [D30]:** RC2, # 12: specify meaning of free flow conditions"

**Formatiert:** Listenabsatz, Aufgezählt + Ebene: 1 + Ausgerichtet an: 0.63 cm + Einzug bei: 1.27 cm

**Formatiert:** Englisch (Vereinigtes Königreich)

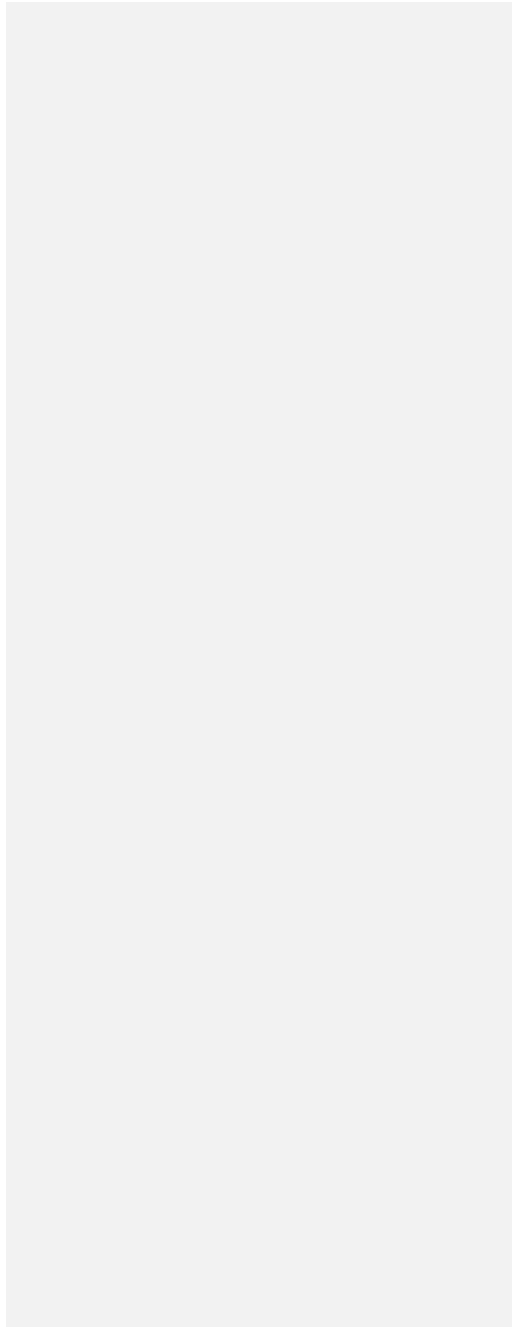
**Kommentiert [D31]:** RC2, #2 and #20: specify objectives and relevance of experiments in both introduction and conclusions

**Formatiert:** Englisch (Vereinigtes Königreich)

forces. Future research is required to quantify the impact of Gurney flaps on dynamic loads, leading edge surface roughness and thus the power output of rotor blades that operate in free flow open field conditions and at high Reynolds numbers.

475

|





Appendix A: Results of the clean case

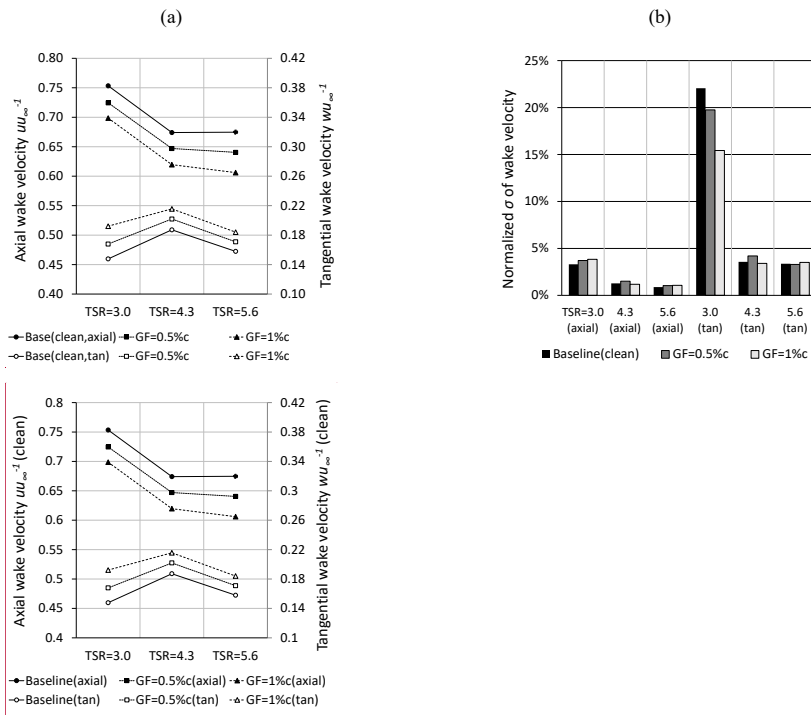


Figure A 1. Clean case at  $r = 0.56R$  and  $\phi = 270^\circ$ . (a) Axial and tangential (tan) wake velocity, normalized by the inflow velocity. (b) Standard deviation of the wake velocity normalized by the average wake velocity.

480

Kommentiert [D32]: RC2, # 11: clarify which curves belong to axial and to tangential velocity

Formatiert: Standard

(a)

(b)

(c)

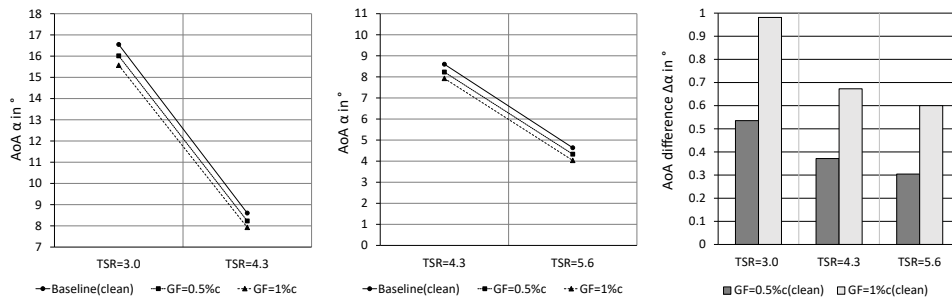


**Figure A 2.** Angles-of-attack in the clean case at  $r = 0.56R$  and  $\varphi = 270^\circ$ . (a) Stall and rated conditions (b) Rated and feather conditions (c) AoA difference between Gurney flap configuration and the baseline.

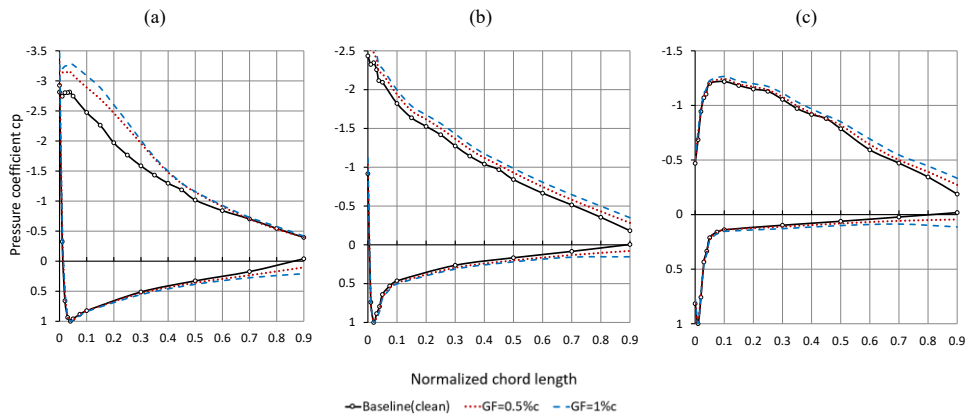


**Figure A 3.** Pressure distribution coefficients in the clean case with respect to different scales at  $r = 0.45R$  and  $\varphi = 270^\circ$ . (a)  $TSR = 3.0$ . (b)  $TSR = 4.3$ . (c)  $TSR = 5.6$ .

485

(a)

(b)

(c)

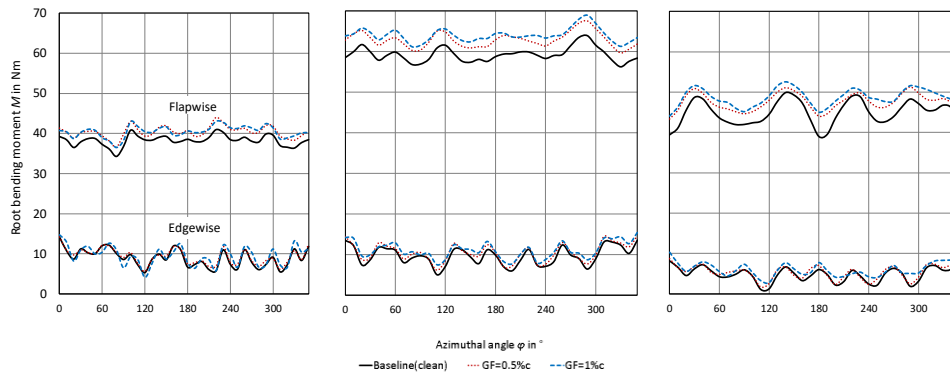


**Figure A 4.** Flapwise and edgewise root bending moments in the clean case. (a)  $TSR = 3.0$ . (b)  $TSR = 4.3$ . (c)  $TSR = 5.6$ .

Formatiert: Standard

Formatiert: Schriftart: Fett

## Appendix B: Uncertainty estimation

The experimental uncertainty of the raw measurement results is expressed by means of the standard deviation,

$$\sigma = \sqrt{\frac{1}{n-1} \sum_{i=1}^n |\mu_i - \bar{\mu}|^2}, \quad (1342)$$

where  $n$  is the number of samples and  $\bar{\mu}$  refers to the average result. The values of  $\sigma$  are rounded up conservatively and thus representative for both tripped and clean baseline cases as well as the GF configurations.

495 **Table 52.** Standard deviation and mean results of tripped baseline as reference values in brackets.

Section	Quantity	<i>TSR</i> = 3.0	<i>TSR</i> = 4.3	<i>TSR</i> = 5.6
3.1	$\sigma(u_w)$ [m·s <sup>-1</sup> ]	0.02 (6.57)	0.02 (6.57)	0.01 (5.02)
	$\sigma(u)$ [m·s <sup>-1</sup> ]	0.20 (4.87)	0.06 (4.55)	0.04 (3.49)
	$\sigma(w)$ [m·s <sup>-1</sup> ]	0.20 (1.06)	0.06 (1.12)	0.03 (0.71)
3.2 <sup>(a)</sup>	$\sigma_{min}(\Delta p)$ [Pa]	2.8 (21.8)	2.6 (102.5)	1.7 (6.1)
	$\sigma_{max}(\Delta p)$ [Pa]	30.0 (-193.6)	5.8 (-269.1)	3.2 (-41.6)
3.3	$\sigma(M_{flap})$ [Nm]	1.9 (36.6)	2.9 (56.5)	2.2 (42.9)
	$\sigma(M_{edge})$ [Nm]	1.0 (8.5)	1.1 (9.1)	0.6 (4.4)

<sup>(a)</sup> Minimum and maximum standard deviation of pressure taps

As expected, the scatter of both the velocity and the pressure data depends on the OP, i.e. it is higher at stall (*TSR* = 3.0), see [Table 5](#)[Table 2](#). Looking at the RBMs, however, the experimental uncertainty of  $\sigma(M_{flap})$  and  $\sigma(M_{edge})$  is influenced by the structural impact of the rotational frequency that the SGs register simultaneously to the aerodynamic forces. Overall, the standard deviation is not significantly influenced by either of the GF configurations.

Subsequently, the 95% confidence interval or so-called random error is computed with

$$\varepsilon = t \cdot \frac{\sigma}{\sqrt{n}} \approx 1.96 \cdot \frac{\sigma}{\sqrt{n}} \quad (1413)$$

505 where  $t$  is the Student's t-distribution (Barlow [et al.](#), 1999).

Formatiert: Schriftart: Nicht Kursiv

Formatierte Tabelle

Formatiert: Links

Formatiert: Schriftart: Kursiv

Formatiert: Schriftart: 10 Pt., Nicht Fett

**Table 63.** 95% confidence interval and mean results of tripped baseline as reference values in brackets.

Section	Quantity	TSR = 3.0	TSR = 4.3	TSR = 5.6
3.1	$\varepsilon(u_w)$ [ms <sup>-1</sup> ]	5.0·10 <sup>-5</sup> (6.57)	5.0·10 <sup>-5</sup> (6.57)	2.8·10 <sup>-5</sup> (5.02)
	$\varepsilon(u)$ [ms <sup>-1</sup> ]	6.1·10 <sup>-3</sup> (4.87)	2.1·10 <sup>-3</sup> (4.55)	1.2·10 <sup>-3</sup> (3.49)
	$\varepsilon(w)$ [ms <sup>-1</sup> ]	7.1·10 <sup>-3</sup> (1.06)	1.8·10 <sup>-3</sup> (1.12)	1.1·10 <sup>-3</sup> (0.71)
3.2 <sup>(a)</sup>	$\varepsilon_{min}(\Delta p)$ [Pa]	4.3·10 <sup>-2</sup> (21.8)	4.0·10 <sup>-2</sup> (102.5)	2.7·10 <sup>-2</sup> (6.1)
	$\varepsilon_{max}(\Delta p)$ [Pa]	5.1·10 <sup>-1</sup> (-193.6)	8.8·10 <sup>-2</sup> (-269.1)	4.8·10 <sup>-2</sup> (-41.6)
3.3	$\varepsilon(M_{flap})$ [Nm]	2.9·10 <sup>-2</sup> (36.6)	4.5·10 <sup>-2</sup> (56.5)	3.4·10 <sup>-2</sup> (42.9)
	$\varepsilon(M_{edge})$ [Nm]	1.5·10 <sup>-2</sup> (8.5)	1.6·10 <sup>-2</sup> (9.1)	9.6·10 <sup>-3</sup> (4.4)

(a) Minimum and maximum confidence interval of pressure taps

Formatierte Tabelle

Formatiert: Links

510 The values of the 95% confidence interval, see [Table 6Table-3](#), are significantly smaller compared to those of the standard deviation ([Table 5Table-2](#)). The reason is the relatively large number of samples, i.e.  $n \approx 3.6 \cdot 10^3$  in terms of the wake velocities,  $u$  and  $w$ , and  $n \approx 1.7 \cdot 10^4$  per azimuthal angle in the remaining cases. Hence, the presented average results are contained by a reasonably small confidence interval.

Formatiert: Schriftart: 10 Pt., Nicht Fett

#### Data availability.

515 Measurement data and results can be provided by contacting the corresponding author.

#### Author contribution

Jörg Alber performed the wind tunnel experiments together with Rodrigo Soto-Valle and the support of all co-authors. Jörg Alber processed the data and prepared the manuscript with the support of Marinos Manolesos and Rodrigo Soto-Valle both of whom contributed with important comments and suggestions to all section of the manuscript.

Formatiert: Überschrift 1, Abstand Vor: 0 Pt., Nach: 0 Pt.

Formatiert: Schriftart: 10 Pt., Nicht Kursiv, Englisch (Vereinigtes Königreich)

#### 520 Competing interests

The authors declare that they have no conflict of interest.

Formatiert: Überschrift 1, Abstand Vor: 0 Pt., Nach: 0 Pt.

## Acknowledgements

The authors would like to acknowledge the constant support of the BeRT project by the researches and the technicians of the Hermann-Föttinger Institut at the Technische Universität Berlin. The authors would also like to acknowledge the technical support of SMART BLADE ®. Rodrigo Soto-Valle would like to thank the support of ANID PFCHA/Becas Chile-DAAD/2016-91645539.

## References

- Alber, J., Pechlivanoglou, G., Paschereit, C. O., Twele, J. and Weinzierl, G.: Parametric Investigation of Gurney Flaps for the Use on Wind Turbine Blades, ASME Turbo Expo, <https://doi.org/10.1115/GT2017-64475>, 2017.
- 530 Bak, C., Zahle, F., Bitsche, R., Kim, T., Yde, A., Henriksen, L.C., Natarajan, A., and Hansen, M.: Description of the DTU 10 MW Reference Wind Turbine, Technical University of Denmark, DTU Wind Energy, 2013.
- Barlow, J. B., Rae, W. H. and Pope, A.: Low-Speed Wind Tunnel Testing, John Wiley & Sons, 3<sup>rd</sup> edition, USA, <https://doi.org/10.2514/2.633>, 1999.
- Bartholomay, S., Fruck, W. L., Pechlivanoglou, G., Nayeri, C. N. and Paschereit, C. O.: Reproducible Inflow Modifications for a Wind Tunnel Mounted Research HAWT, ASME Turbo Expo, <https://doi.org/10.1115/GT2017-64364>, 2017.
- 535 Bartholomay, S., Marten, D., Martínez, M. S., Alber, J., Pechlivanoglou, G., Nayeri, C. N., Paschereit, C. O., Klein, A. C., Lutz, T., and Krämer, E.: Cross-Talk Compensation for Blade Root Flap- and Edgewise Moments on an Experimental Research Wind Turbine and Comparison to Numerical Results, ASME Turbo Expo, <https://doi.org/10.1115/GT2018-76977>, 2018.
- 540 Bechert, D. W., Meyer, R. and Hage, W.: Drag reduction of airfoils with miniflaps - Can we learn from dragonflies?, AIAA Paper, <https://doi.org/10.2514/6.2000-2315>, 2000.
- Burton, T., Jenkins, N., Sharpe, D. and Bossanyi, E.: Wind Energy Handbook, 2<sup>nd</sup> edition, Wiley-Interscience, UK, <https://doi.org/10.1002/9781119992714>, 2011.
- 545 Cuerva, A., Tejero, Sanz-Andrés, A. and Navarro, J.: On multiple-path sonic anemometer measurement theory, Exp. Fluids, Bd. 34, S. 345–357, <https://doi.org/10.1007/s00348-002-0565-x>, 2003.
- Drela, M.: XFOIL: An Analysis and Design System for Low Reynolds Number Airfoils, MIT: Massachusetts Institute of Technology, [https://doi.org/10.1007/978-3-642-84010-4\\_1](https://doi.org/10.1007/978-3-642-84010-4_1), 1989.
- 550 Fischer, J.: BWKA-1.5 TUB - Blades with Servo controlled Flaps, Smart Blade ®, Berlin, Germany, 2015.
- Fuglsang, P., Antoniou, I., Sorensen, N., Aagaard, M., Helge A.: Validation of a wind tunnel testing facility for blade surface pressure measurements. Forskningscenter Risoe, Risoe-R, No. 981(EN), Denmark, 1998.

Formatiert: Überschrift 1, Abstand Vor: 0 Pt., Nach: 0 Pt.

Formatiert: Überschrift 1

Formatiert: Einzug: Erste Zeile: 0 cm

Formatiert: Einzug: Erste Zeile: 1.27 cm

Formatiert: Schriftart:

- 555 Giguère, P., Lemayt, J. and Dumas, G.: Gurney flap effects and scaling for low-speed airfoils, AIAA Paper, <https://doi.org/10.2514/6.1995-1881>, 1995.
- Gruschwitz, E. and Schrenk, O.: A simple method for increasing the lift of airplane wings by means of flaps, Zeitschrift fuer Flugtechnik und Motorluftschiffahrt, Vol 23 No 20, 1933.
- Hand, M., Simms, D., Fingersh, L., Jager, D., Cotrell, J., Schreck, S. and Larwood, S.: Unsteady aerodynamics experiment phase VI: wind tunnel test configurations and available data campaigns, National Renewable Energy Lab, <https://doi.org/10.2172/15000240>, 2001.
- 560 Hansen, M. O. L.: Aerodynamics of Wind Turbines, 2nd Edition, Earthscan, UK, <https://doi.org/10.4324/9781849770408>, 2015.
- Herráez, I., Daniele, E. and Schepers, J. G.: Extraction of the wake induction and angle of attack on rotating wind turbine blades from PIV and CFD results, Wind Energy Science, <https://doi.org/10.5194/wes-3-1-2018>, 2018.
- 565 Holst, D., Pechlivanoglou, G., Kohlrausch, C. T., Nayeri, C. N. and Paschereit, C. O.: sHAWT Design: Airfoil Aerodynamics Under the Influence of Roughness, ASME Turbo Expo, <https://doi.org/10.1115/GT2016-56377>, 2016.
- Houghton, E. L., Carpenter, P.W., Collicott, S. H. and Valentine, D. T.: Aerodynamics for Engineering Students, 6<sup>th</sup> edition, Aerodynamics for Engineering Students, <https://doi.org/10.1016/C2009-0-63882-4>, 2013.
- 570 Kentfield, J.: The Influence of Free-Stream Turbulence Intensity on the Performance of Gurney-Flap Equipped Wind-Turbine Blades, Wind Engineering, <https://www.jstor.org/stable/43749607>, 1996.
- Kheir-~~A~~ldeen, M., and Hamid, A.: Experimental Study to the Effect of Gurney Flap on the Clark Y-14 Airfoil Wing Model, International Journal of Innovation and Scientific Research, ISSN 2351-8014, 2014
- Klein, A. C., Bartholomay, S., Marten, D., Lutz, T., Pechlivanoglou, G., Nayeri, C. N., Paschereit, C. O., and Krämer, E.: 575 About the suitability of different numerical methods to reproduce model wind turbine measurements in a wind tunnel with a high blockage ratio, Wind Energy Science, <https://doi.org/10.5194/wes-3-439-2018>, 2018.
- Liebeck, R. H.: Design of subsonic airfoils for high lift, Journal of Aircraft, <https://doi.org/10.2514/3.58406>, 1978.
- Marten, D., Wendler, J., Pechlivanoglou, G., Nayeri, C. N. and Paschereit, C. O.: Development and Application of a Simulation Tool for Vertical and Horizontal Axis Wind Turbines, ASME Turbo Expo, <https://doi.org/10.1115/GT2013-94979>, 2013.
- 580 Mueller-Vahl, H., Pechlivanoglou, G., Pechlivanoglou, G., Nayeri, C. N. and Paschereit, C. O.: Vortex Generators for Wind Turbine Blades: A combined Wind Tunnel and Wind Turbine Parametric Study, ASME Turbo Expo, GT2012-69197, <https://doi.org/10.1115/GT2012-69197>, 2012.
- 585 Pechlivanoglou, G., Fuehr, S., Nayeri, C. N. and Paschereit, C. O.: The Effect of Distributed Roughness on the Power Performance of Wind Turbines, ASME Turbo Expo, <https://doi.org/10.1115/GT2010-23258>, 2010.
- Pechlivanoglou, G., Philippidis T. P., Vey, S., Eisele, O., Nayeri, C. N. and Paschereit, C. O.: Vortex Generators for Wind

Formatiert: Hochgestellt

Formatiert: Englisch (Vereinigtes Königreich)

Formatiert: Einzug: Links: 0 cm

Turbine Blades: Wind Tunnel Tests, Field Simulations and Structural Analysis, ASME Turbo Expo, RZGM2013-34, 2013.

590 Rooij, R. P. J. O. M. van and Timmer, W. A.: Roughness Sensitivity Considerations for Thick Rotor Blade Airfoils, AIAA Paper 2003-0350, <https://doi.org/10.2514/6.2003-350>, 2003.

Schatz, M., Günther, B., and Thiele, F. Computational modeling of the unsteady wake behind Gurney-flaps, AIAA Paper, <https://doi.org/10.2514/6.2004-2417>, 2004.

595 Snel, H., Schepers, J. G., and Siccama, N. B.: Mexico project: The database and results of data processing and interpretation, AIAA Paper, <https://doi.org/10.2514/6.2009-1217>, 2009.

Soto-Valle, R., Bartholomay, S., Alber, J., Manolesos, M., Nayeri, C. N. and Paschereit, C. O.: Determining the Angle of Attack along a Wind Turbine Rotor Blade in Wind Tunnel Experiments, Wind Energy Science, <https://doi.org/10.5194/wes-2020-35>, 2020.

600 Storms, B. L. and Jang, C. S.: Lift Enhancement of an Airfoil Using a Gurney Flap and Vortex Generators, Journal of Aircraft, Vol. 31, No. 3, <https://doi.org/10.2514/3.46528>, 1994.

Vestas: Lift production with Vortex Generators and Gurney Flaps, <https://www.vestas.com/en/campaignsites/aerodynamicupgrades/home#>, (last access: ~~01-12 September June~~ 2020).

605 Vey, S., Marten, D., Pechlivanoglou, G., Nayeri, C. and Paschereit, C. O.: Experimental and Numerical Investigations of a Small Research Wind Turbine, AIAA Paper, <https://doi.org/10.2514/6.2015-3392>, 2015.

Weber, F.I., Durgin, W. W. and Iohari, H.: Circulation measurements about a rapidly pitching airfoil using an ultrasonic system, AIAA Paper, <https://doi.org/10.2514/6.1995-2269>, 1995.

610 Wilcox, B. J., White, E. B. and Maniaci, D. C.: Roughness Sensitivity Comparisons of Wind Turbine Blade Sections, Sandia Report, SAND2017-11288, <https://doi.org/10.2172/1404826>, 2017.

Zhang, Y., van Zuijlen, A. and van Bussel, G.: The MEXICO rotor aerodynamic loads prediction: ZigZag tape effects and laminar-turbulent transition modeling in CFD, Journal of Wind Engineering and Industrial Aerodynamics, <https://doi.org/10.1016/j.jweia.2017.06.002>, 2017.

Formatiert: Einzug: Erste Zeile: 1.27 cm

Formatiert: Einzug: Erste Zeile: 1.27 cm

Feldfunktion geändert

Formatiert: Einzug: Links: 0 cm

Formatiert: Einzug: Links: 0 cm, Erste Zeile: 1.27 cm

Feldfunktion geändert